P1: SFK/UKS P2: SFK Trim: 247mm × 174mm Top: 14.762mm Gutter: 18.98mm
CUUK1151-02 CUUK1151-Olafsen 978 0 521 11590 2 March 28, 2010 6:20

2

Computational methods to study jammed systems

CARL F. SCHRECK AND COREY S. O'HERN

1 Introduction

Jammed materials are ubiquitous in nature and share several defining characteristics. They are disordered, yet solid-like with a nonzero static shear modulus. Jammed systems typically exist in metastable states with structural and mechanical properties that depend on the procedure used to create them. There are a number of different routes to the jammed state, including compressing systems to densities near random close packing [1], lowering the applied shear stress below the yield stress [2], and quenching temperature below the glass transition for the material [3]. Examples of jammed and glassy particulate systems include dense colloidal suspensions [4], attractive glasses and gels [5], static packings of granular materials [6], and quiescent foams [7] and emulsions [8]. Due to space constraints, we will limit our discussion to athermal jammed systems in which thermal energy at room temperature is unable to induce local rearrangements of particles. We note though that there are deep connections [9] between athermal jammed systems and thermal, glassy systems [10]. An important open problem in the field of jammed materials is identifying universal features that are not sensitive to the particular path in parameter space taken to create them.

In this contribution, we will review the computational techniques used to generate athermal jammed systems and characterize their structural and mechanical properties. We will focus on frictionless model systems that interact via soft, pairwise, and purely repulsive potentials. (Computational studies of frictional granular materials will be the focus of Chapter 5.) The methods for generating jammed particle packings discussed here are quite general and can be employed to study both two- and three-dimensional systems; both monodisperse and polydisperse systems; a spectrum of particle shapes, including spheres, ellipsoids, and rods; and a variety of boundary conditions and applied stress.

The remainder of the chapter will be organized as follows. In Section 2, we will review computational methods for creating static particle packings. Many prior studies of jamming have focused on spherical particles under isotropic compression. We will therefore describe how packing-generation methods can be generalized, with a particular emphasis on grains with nonspherical shapes. This review will be restricted to completely jammed, *mechanically stable* (MS) packings, and thus in Section 3, we will define mechanical stability of particle packings in terms of the normal modes of the dynamical matrix [11]. In Section 4, we will describe many of the computational measurements that can be performed to characterize the structural and mechanical properties of jammed packings, including the pair distribution function, structure factor, translational and orientational order parameters, correlation functions, spectra of vibrational modes, and elastic moduli.

2 Methods to generate static-particle packings

Computational methods to generate jammed particle packings fall into two general categories: 'hard' [12] and 'soft' [13], [14], [15] particle methods. Hard particle methods strictly enforce the constraint that particles cannot overlap; these include the Lubachevsky–Stillinger algorithm of binary collisions between elastic particles coupled with compression [16], single-particle and collective Monte-Carlo moves with successive compressions, and various geometrical techniques [17], [18], [19].

In this contribution, we will review two soft-particle packing-generation techniques: (1) the *isotropic compression* method in which we successively compress or decompress the system followed by energy relaxation until all particles are just touching and (2) the *applied shear* method in which we generate just-touching particle packings at arbitrary values of shear strain. We focus on soft-particle packing-generation methods for several reasons. First, the structural and mechanical properties can be studied as a function of overcompression $\phi - \phi_J$, where ϕ_J is the jamming packing fraction, which allows numerical results to be compared to experiments on foams, emulsions, and granular materials. Second, features of hard-particle MS packings can be recovered from soft-sphere packings in the just-touching limit. Finally, many hard-particle methods yield locally jammed packings, which are not mechanically stable. In contrast, soft-particle methods, which satisfy the constraints of force and torque balance on all grains, reliably produce mechanically stable packings.

2.1 Isotropic compression

The isotropic compression method for soft particles consists of initializing the system in a dilute, fluid-like configuration and successively compressing/

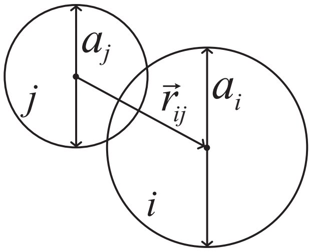

Figure 2.1 Schematic showing the definition of the contact distance σ_{ij} for two disks i and j, with diameters a_i and a_j and center-to-center separation r_{ij}. The two particles overlap when $r_{ij} < \sigma_{ij}$, where $\sigma_{ij} = (a_i + a_j)/2$ is the average diameter.

decompressing the system followed by energy relaxation to the nearest local minimum. The method terminates at packing fraction ϕ_J when all particles (except floater particles that are not locally stable) achieve force and torque balance with infinitesimal particle overlaps. In these studies, we will employ pairwise, short-range repulsive interactions between particles. The pair potential $V(r_{ij}/\sigma_{ij})$, where r_{ij} is the center-to-center separation and σ_{ij} is the contact distance between grains i and j, is positive if particles are overlapped ($r_{ij} < \sigma_{ij}$) and zero otherwise. Thus, the packings possess nonzero, but infinitesimal pressure and potential energy at jamming.

We will focus on two forms for the interaction potential: the repulsive spring potential V_{s} in (2.1) and the repulsive Lennard–Jones potential in (2.2):

$$V_{\mathrm{s}}(r_{ij}) = \frac{\epsilon}{\alpha}\left(1 - \frac{r_{ij}}{\sigma_{ij}}\right)^{\alpha} \Theta\left(\frac{\sigma_{ij}}{r_{ij}} - 1\right), \tag{2.1}$$

$$V_{\mathrm{RLJ}}(r_{ij}) = \epsilon\left[\left(\frac{\sigma_{ij}}{r_{ij}}\right)^{12} - 2\left(\frac{\sigma_{ij}}{r_{ij}}\right)^{6} + 1\right] \Theta\left(\frac{\sigma_{ij}}{r_{ij}} - 1\right), \tag{2.2}$$

where $\alpha = 2$ ($\alpha = 5/2$) correspond to the linear (Hertzian) repulsive spring potential, $\Theta(x)$ is the Heaviside step function, which ensures that particles only interact when they overlap. For spherical particles, the contact distance is simply the average of their diameters $\sigma_{ij} = (a_i + a_j)/2$, as shown in Figure 2.1. The contact distance σ_{ij} for nonspherical grains, which depends on $\hat{r}_{ij}$ and the orientations of grains i and j, will be discussed in detail in Section 2.3.2. The total potential energy per particle for the system is given by $V = N^{-1} \sum_{i,j} V(r_{ij})$.

The isotropic compression method can be viewed in terms of the potential energy landscape $V(\vec{\xi})$ of the system, as shown in Figure 2.2. All possible configurations of N particles, each denoted by $\vec{\xi} = (\vec{r}_1, \vec{r}_2, \ldots, \vec{r}_N)$, yield a value of the potential energy per particle $V(\vec{\xi})$. Static, force- and torque-balanced packings correspond to local minima in the potential energy landscape. Jammed packings

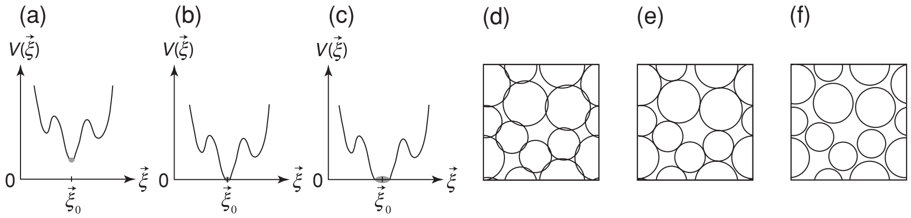

Figure 2.2 Schematic of the isotropic compression method to create jammed packings. In panels (a)–(c), we show the potential energy landscape $V(\vec{\xi})$ in the vicinity of the static granular packings (at point $\vec{\xi}_0$ in configuration space) in panels (d)–(f). If the system exists in a nonoverlapped configuration (panel (f)) with gaps between particles and $V = 0$, it will be compressed followed by energy minimization. If the system exists in an overlapped configuration (panel (d)) at a local potential energy minimum with $V > 0$, it will be decompressed followed by energy minimization. When the system switches between the cases displayed in panels (d) and (f), the compression/decompression increment is decreased. The process stops when the system exists in a static packing at a local potential energy minimum that is infinitesimally above zero.

correspond to minima with $V(\vec{\xi}) \gtrsim 0$. During the packing-generation process, if there are significant particle overlaps (Figure 2.2(d)) and the energy of the system at a local minimum is nonzero (Figure 2.2(a)), the system will be subsequently decompressed. If the potential energy of the system is zero (Figure 2.2(c)) and gaps exist between particles (Figure 2.2(f)), the system will be compressed at the next step. The increment by which the packing fraction ϕ is changed at each compression or decompression step is gradually decreased. After a sufficiently large number of steps, a jammed packing with infinitesimal overlaps (Figure 2.2(e)) and potential energy $V \gtrsim 0$ (Figure 2.2(b)) is obtained.

The isotropic compression method for generating jammed particle packings consists of four basic steps: (1) initialization of particle positions and orientations, (2) compression or decompression of the system, (3) relaxation of the potential energy to the nearest local minimum, and (4) repetition of steps (2) and (3) until a jammed packing with infinitesimal overlaps is obtained. We will describe the implementation of these steps in detail here:

Step (1) Choose an initial configuration for N particles in the simulation cell. This is typically accomplished by assigning each particle a random position and orientation, in the case of nonspherical particles, in the simulation cell. For the repulsive Lennard–Jones interaction potential, random initial configurations without significant particle overlaps must be used. If the initial packing fraction, ϕ_0, is well below the mean jammed packing fraction, $\langle \phi_J \rangle$, the initial conditions will not bias the final set of packings. The results obtained for $\phi_0 > \langle \phi_J \rangle$ and for $\phi_0 < \langle \phi_J \rangle$ only show small differences for frictionless grains, but these differences are important and should be studied in more detail in future studies. When choosing orientations, directors can be selected randomly from a uniform distribution on the unit disk (sphere) in 2D (3D).

Step (2) Compress the system (or increase particle sizes uniformly) if it is below the jamming point ($V < V_{\mathrm{tol}}$) or decompress the system (or decrease particle sizes uniformly) if it is above the jamming point ($V > 2V_{\mathrm{tol}}$). V_{tol} is the potential energy threshold that dictates how close the final packing is to the point at which all particles are just touching. We typically consider $V_{\mathrm{tol}} = 10^{-16}$ (where V is normalized by the energy-scale parameter ϵ) based on numerical precision. We must choose the initial packing fraction increment $\Delta\phi_0$ to be sufficiently small so that it does not influence the jammed packing fraction, but also large enough to efficiently generate jammed packings. Previous studies have used $\Delta\phi_0 = 10^{-4}$ [14], [15]. The packing fraction increment is successively decreased to locate ϕ_J. If the potential energy of the system at successive compressions or decompressions $n - 1$ and n satisfy $V_{n-1} > 2V_{\mathrm{tol}}$ and $V_n < V_{\mathrm{tol}}$ or $V_{n-1} < V_{\mathrm{tol}}$ and $V_n > 2V_{\mathrm{tol}}$, the step size is halved. Otherwise it remains at the current value of $\Delta\phi$.

Step (3) Minimize the total potential energy of the system after each compression or decompression step to find a local potential energy minimum. The energy minimization can be performed in several ways, including (a) numerical energy minimization procedures, such as the conjugate-gradient technique [20] and (b) molecular dynamics (MD) simulations with dissipative forces proportional to velocity. The conjugate-gradient method is a numerical scheme that begins at a given point in configuration space and moves the system to the nearest local potential energy minimum without traversing any energy barriers [20]. In contrast, molecular dynamics with finite damping is not guaranteed to find the nearest local potential energy minimum since kinetic energy is removed from the system at a finite rate. The system can thus surmount a sufficiently low energy barrier. A comparison of these two methods provides important geometric information about the width of basins and heights of energy barriers separating the basins in the energy landscape.

In the molecular-dynamics method, each particle i obeys Newton's equations of motion:

$$m\vec{a}_i = \sum_{j \neq i} \left[-\frac{dV(r_{ij})}{dr_{ij}} - b\vec{v}_{ij} \cdot \hat{r}_{ij} \right] \hat{r}_{ij}, \tag{2.3}$$

where $\vec{a}_i$ is the acceleration of particle i, $\vec{v}_{ij}$ is the relative velocity of particles i and j, $\hat{r}_{ij}$ is the unit vector connecting the centers of these particles, and b is the damping coefficient. In the infinite-dissipation limit, $b \to \infty$, the potential energy cannot increase during a molecular-dynamics relaxation, and thus the molecular-dynamics and conjugate-gradient methods should give very similar

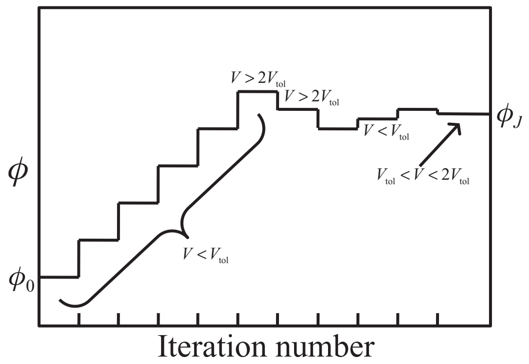

Figure 2.3 Schematic of the isotropic compression method for creating jammed particle packings. The system is initialized at a packing fraction ϕ_0 below the jamming onset ϕ_J. After a series of compressions and decompressions of decreasing amplitude, the jamming onset ϕ_J is identified with total potential energy per particle at a local energy minimum that satisfies $V_{\mathrm{tol}} < V < 2V_{\mathrm{tol}}$.

results. We note, however, that even in this limit the two methods are not equivalent because there may be more than one energy minimum accessible from a given point in configuration space without traversing an energy barrier.

For the conjugate-gradient method, we terminate the minimization process when either of the following two conditions on the potential energy per particle V is satisfied: (a) two successive conjugate-gradient steps t and $t+1$ yield nearly the same energy value, $(V_{t+1} - V_t)/V_t < \delta = 10^{-16}$; or (b) the potential energy per particle at the current step is extremely small, $V_t < V_{\mathrm{min}} = 10^{-16}$. Since the potential energy oscillates in time in the molecular-dynamics method, condition (a) is replaced by the requirement that the relative potential-energy fluctuations satisfy the inequality $\langle (V - \langle V \rangle)^2 \rangle^{1/2} / \langle V \rangle < \delta$. Stopping criteria based on the rms or maximum total force on the particles can also be implemented.

Step (4) The packing-generation procedure terminates when the potential energy at a local energy minimum satisfies $V_{\mathrm{tol}} < V < 2V_{\mathrm{tol}}$. Using this method, we are able to locate the jamming threshold in packing fraction ϕ_J to within 10^{-8} for each static packing. A schematic of the dynamics of the packing fraction during the compression method is shown in Figure 2.3. This method can be performed for many different initial configurations to generate an ensemble of jammed packings.

2.2 Applied shear strain

Athermal jammed systems can also be generated in the presence of applied shear stress or strain. In fact, recent experimental [21], simulation [22], and theoretical [23], [24] studies have emphasized that the form of stress correlations in jammed

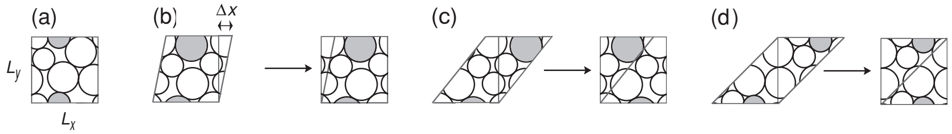

Figure 2.4 Schematic diagram of shear-periodic boundary conditions. (a) Static packing with $N = 6$ particles confined to a $L_x \times L_y$ box with shear strain $\gamma = \Delta x / L_y = 0$. The shading indicates a given particle in the primary cell and its image. (b) Static packing in a unit cell with $\gamma = 0.2$. Note that at arbitrary γ, a given particle in the primary cell is not directly above (or below) its image. (c) Static packing at $\gamma = 0.8$, which shows that configurations at γ and $1 - \gamma$ are related by an inversion about the vertical (shear-gradient) direction. (d) Static packing in (a) at $\gamma = 1$, which is identical to standard periodic boundary conditions. Thus shear-periodic boundary conditions have unit period. Adapted from reference [28].

packings created by isotropic compression and shear are fundamentally different, with longer ranged spatial correlations along the compressive direction in sheared systems. In experiments, simple shear can be implemented using planar [25] or Couette geometries [26]. In simulations, bulk planar shear flow can be realized using Lees–Edwards or shear-periodic boundary conditions [27]. In Figure 2.4, we show a schematic diagram of shear-periodic boundary conditions implemented in 2D. In each panel, the top (bottom) image cells are shifted by $\Delta x = \gamma L_y$ to the right (left), where γ is the shear strain and L_y is the dimension of the simulation cell in the shear gradient direction.

Note that shear-periodic boundary conditions are identical at $\gamma = x$ and $1 - x$ and have unit period as shown in Figure 2.4; thus, we only need to study the range $\gamma = 0$ to 0.5 to generate static packings over the full range of shear strain. Prior studies of jammed systems have focused on isotropically compressed packings at $\gamma = 0$ [13], whereas there are relatively few studies of sheared packings at nonzero γ [28]. To generate anisotropic static packings, the region $\gamma = [0, 0.5]$ can be divided into small shear strain intervals, e.g. $\Delta\gamma = 10^{-2}$. At each sampled shear strain γ_s, the four-step compression/decompression method discussed in Section 2.1 can be implemented to generate static, just-touching particle packings. That is, the particles' positions and orientations are chosen randomly, and the system is subjected to a sequence of compressions and decompressions with decreasing amplitude, each followed by energy relaxation at a *fixed shear strain*, until the energy of the system falls within a prescribed window. When this procedure is repeated many times for different γ_s and independent initial conditions, we can generate ensembles of packings over a series of discrete strains γ_s.

To create continuous maps of static packings between sampled shear strains γ_s and γ_{s+1}, we can apply n successive shear strains to each static packing at

γ_s of size $\delta\gamma = \Delta\gamma/n$, each followed by the compression packing-generation process described in Section 2.1. Shear strain steps $\delta\gamma$ are applied by shifting the x-coordinate of each particle i according to:

$$x_i \rightarrow x_i + \delta\gamma y_i \tag{2.4}$$

in conjunction with shear-periodic boundary conditions. A similar procedure can also be performed to study the continuous set of static packings for shear strains in the opposite direction between γ_s and γ_{s-1}. Note that this procedure generates a series of static packings over a range of shear strain at fixed *zero pressure*, not at fixed volume as in previous studies of quasistatically sheared Lennard–Jones [29] and other model glasses [30].

A schematic of the process for generating the continuous set of static packings between shear strains γ_s and γ_{s+1} (or γ_s and γ_{s-1}) is shown in Figure 2.5. Panels (a) and (b) show two possible evolutions of the potential energy landscape following a shear strain step $\delta\gamma$. In (a), no particle rearrangement event occurs and the local minimum (1) can be continuously deformed into local minimum (4) by applying shear strain $\delta\gamma$. The dynamics of the system can be summarized as follows: we apply a shear strain $\delta\gamma$ to the initial static packing with strain γ (1), which shifts the point in configuration space and the potential energy landscape (2). The energy is then minimized at fixed shear strain $\gamma + \delta\gamma$ (3), and the system is decompressed (or compressed, followed by energy minimization) to bring it to a static packing with infinitesimal overlap (4). The static packings at shear strains γ (1) and $\gamma + \delta\gamma$ (4) are overlayed in panel (c). Note that the particle contact networks are identical at γ (gray) and $\gamma + \delta\gamma$ (black).

In contrast, Figure 2.5(b) shows the evolution of the system when at least one particle rearrangement occurs following a shear strain step. In this case, a shear strain $\delta\gamma$ is applied to a static packing at shear strain γ (1), and the system moves in configuration space so that it exists in the basin of a new local minimum (2). Upon energy minimization at fixed $\gamma + \delta\gamma$, the system moves to an unjammed packing (3). Following compression and energy minimization, the system resides in a new static packing at $\gamma + \delta\gamma$ (4) that is not continuously related to the static packing at γ. In Figure 2.5(d), we overlay the static packings at γ (gray) and $\gamma + \delta\gamma$ (black) and show that the particle contact networks are not the same.

For each distinct static packing at γ_s, we can monitor the particle contact network as the system evolves toward γ_{s+1} (and γ_{s-1}) and identify any changes that occur. If there are changes in the particle contact network, physical quantities such as the jamming packing fraction ϕ_J, pressure, and shear stress (and their derivatives) are discontinuous. For example, in Figure 2.6(b), we show a discontinuity in ϕ_J at $\gamma_s < \gamma^* < \gamma_{s+1}$, where a particle rearrangement event occurs. $\delta\gamma$ can be tuned to eliminate as many of the particle rearrangement events as possible.

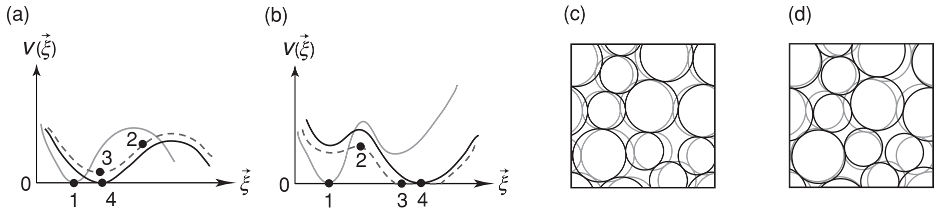

Figure 2.5 Schematic of the evolution of the potential energy landscape during quasistatic shear at fixed zero pressure from shear strain γ to $\gamma + \delta\gamma$. In (a), the system evolves continuously from the local minimum at shear strain γ (1) to the one at $\gamma + \delta\gamma$ (4) because there are no particle rearrangement events during the shear strain interval. In contrast, in (b) the system undergoes particle rearrangement events during the strain interval $\delta\gamma$, and therefore it resides in a fundamentally different potential energy minimum at $\gamma + \delta\gamma$ (4) compared to the one at γ (1). Snapshots of the static packings at shear strain γ (gray) and $\gamma + \delta\gamma$ (black) are superimposed in (c) and (d), which correspond to the potential energy landscape dynamics in (a) and (b), respectively. In (d), three of the original contacts are removed and four new contacts are generated as a result of the particle rearrangements that occurred during the strain interval $\delta\gamma$. Adapted from reference [28].

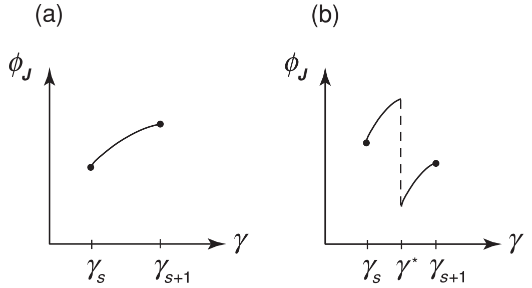

Figure 2.6 Schematic of the evolution of the jamming packing fraction ϕ_J during the shear strain interval γ_s to γ_{s+1}. In (a) the particle contact network does not change from γ_s to γ_{s+1}, while in (b), it does at γ^*. Adapted from reference [28].

In Figure 2.6(a), we show the continuous evolution of ϕ_J between γ_s and γ_{s+1} when there are no particle rearrangement events. This continuous evolution of ϕ_J represents a portion of a ‘geometric family’ of static packings all with the same particle contact network that exist over a continuous range of shear strain from γ_s to γ_{s+1}. In Figure 2.7, we show results where we have pieced together these continuous segments to construct nearly all of the geometric families over the full range of shear strain for a small $N = 10$ frictionless granular system [28]. Note that even though there are an infinite number of static packings over the continuous range of shear strain, there are a *finite* number of geometric families that can be counted.

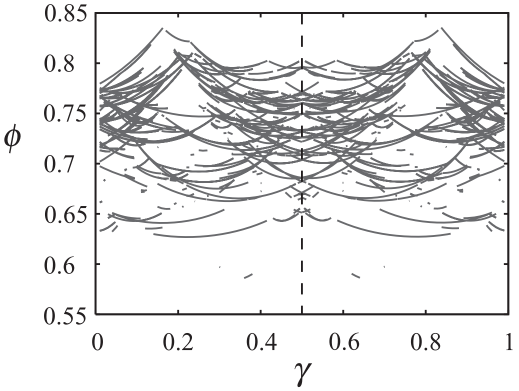

Figure 2.7 The solid lines show the jammed packing fraction ϕ_J versus shear strain γ for different geometric families. The continuous geometric families of static packings possess the same contact network over a given range of shear strain. When the solid line breaks, the continuous family becomes unstable and the particle contact network changes. The families are symmetric with respect to reflection about $\gamma = 0.5$ (dashed vertical line). This figure is adapted from reference [28].

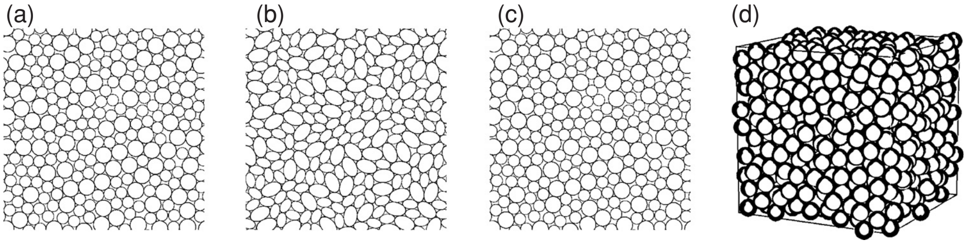

Figure 2.8 Snapshots of static particle packings created using the isotropic compression method in Section 2.1 (a) 2 : 1 (fraction of small particles to fraction of large particles) mixture of bidisperse disks with diameter ratio $\sigma_l/\sigma_s = 1.4$, (b) 2 : 1 mixture of bidisperse ellipses with ratio of major axes $a_l/a_s = 1.4$, (c) polydisperse mixture of disks with a flat probability distribution for the diameters between σ_s and $1.4\sigma_s$, and (d) monodisperse spheres.

2.3 Other important variables

The packing-generation methods described in Sections 2.1 and 2.2 can be generalized to study packings as a function of a number of important variables that affect their structural and mechanical properties. These parameters include the dimension (2D, 3D, and higher dimensions) [31], particle size distribution [32], boundary conditions [28], and particle shape [16]. In Figure 2.8, we show several different types of static granular packings that we generated in prior studies, including (a) bidisperse ($2N/3$ small and $N/3$ large) disks with diameter ratio $\sigma_l/\sigma_s = 1.4$ [13],

(b) bidisperse (same composition as in (a)) ellipses with ratio of the major axes $a_l/a_s = 1.4$ [33], (c) polydisperse disks with a uniform distribution of particle sizes with width $0.4\sigma_s$ and mean $1.2\sigma_s$ [34] (labeled polydispersity $p = 1.4$), and (d) monodisperse spheres [13].

Important control variables for the particle size include the diameter ratio and relative number of large and small particles for bidisperse, tridisperse, or other systems with discrete particle species, and properties of the particle size distribution for continuously polydisperse systems, i.e. the mean and rms width for uniform, normal, and log-normal size distributions.

The packing-generation procedures we discussed in Sections 2.1 and 2.2 employ periodic boundary conditions at either fixed zero pressure (Section 2.1) or fixed shear strain (Section 2.2). However, it is straightforward to generalize these methods to systems with smooth or rough fixed walls [2], constraints imposed at the boundaries, such as constant stress [35], and gravity [36].

In addition, particle shape is a key variable that significantly affects the jamming transition in particle packings. Introducing nonspherical shapes does not significantly alter the steps in the packing-generation procedures in Sections 2.1 and 2.2. However, even for simple anisotropic shapes, such as ellipses, the calculation of the contact distance between grains i and j is nontrivial since it depends on $\hat{r}_{ij}$ and grain orientations.

2.3.1 Particle shape

Recent studies have suggested that particle shape strongly influences the nature of the jamming transition [33], [37]. Specifically, the scaling of the shear modulus with packing fraction and the shape of the vibrational spectrum are fundamentally different from that for spherical particles. Thus, the ability to create jammed packings of nonspherical particles and study the effects of particle shape on the jamming transition are clearly timely and important research efforts.

Particle shape is an enormous parameter space. In this discussion, we will focus on three relevant shape variables, all of which are captured in Figure 2.9: (1) convex (a) versus concave (b)–(d) shapes, (2) rigid anisotropic grains with different degrees of symmetry constructed by fusing spherical particles together (b)–(d), and (3) ellipsoidal particles (a). The jamming behavior of convex vs. concave particle shapes can be contrasted by studying ellipsoidal vs. rigid linear n-mers, where n is the number of spherical particles that have been fused together. Fused colloidal silica spheres can now be made reliably in a variety of shapes, including dimers and trimers. The benefit of studying rigid anisotropic particles formed from fusing spherical particles together, such as linear n-mers, asymmetric n-mers, and nonlinear n-mers, is that the contact distance, forces, and interaction energy between grains i and j can be calculated by assuming that the grains are

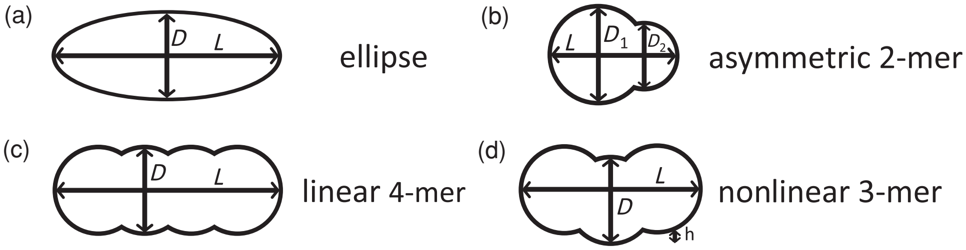

Figure 2.9 The packing-generation methods described in Section 2 can be employed in systems with anisotropic particle shapes, such as ellipsoids, linear n-mers, asymmetric n-mers, and nonlinear n-mers. Examples of geometric parameters that can be tuned are the aspect ratio $\alpha = L/D$, asymmetry $s = D_2/D_1$ for asymmetric dimers, and bending angle $c = h/L$ for nonlinear trimers.

composed of a series of spherical particles. The calculation of the contact distance and all other quantities is trivial for spherical particles. In contrast, ellipsoidal particles have simple nonspherical shapes, yet the calculation of the contact distance, interaction forces, and other quantities is quite complicated.

The packing-generation procedures discussed in Sections 2.1 and 2.2 require the specification of a potential energy function $V(\vec{\xi})$ and its first derivatives $\partial V(\vec{\xi})/\partial \vec{\xi}$, where $\vec{\xi}$ represents the configurational degrees of freedom, e.g. $\vec{\xi} = \{x_i, y_i, \theta_i\}$ with $i = 1, \ldots, N$ for ellipses, where θ_i is the angle between $\hat{x}$ and the long axis of grain i. We also assume that the potential energy only depends on r_{ij}/σ_{ij}, where σ_{ij} is the contact distance between grains i and j. For spherical particles, the contact distance $\sigma_{ij} = (\sigma_i + \sigma_j)/2$ is a constant (average diameter) that depends on the particle species in polydisperse systems and the only relevant derivatives of the potential energy are $\partial r_{ij}/\partial r_i$, where $r = x, y, z$. For nonspherical particles, the contact distance is not constant and depends on $\hat{r}_{ij}$ and the orientations of particles i and j. For ellipsoidal particles, we define σ_{ij} as the true contact distance: the center-to-center separation r_{ij} at which two particles come into contact at fixed orientation. The definition of σ_{ij} for two ellipses i and j with orientations $\hat{\mu}_i$ and $\hat{\mu}_j$ and center-to-center separation r_{ij} is shown in Figure 2.10. The method for calculating σ_{ij} for ellipsoidal particles is described in detail below.

2.3.2 Contact distance for ellipsoidal particles

To generate static packings of ellipsoidal particles using soft-particle methods, we must be able to calculate the potential energy $V(\vec{\xi})$ and its derivatives for general configurations $\vec{\xi}$, which involves determining the contact distance σ_{ij} and its derivatives. This section will provide a survey of the techniques for calculating σ_{ij} in both 2D and 3D. In 3D, we will limit the discussion to spheroids – ellipsoids with one axis of symmetry. A spheroid in which the long (short) axis is the axis of

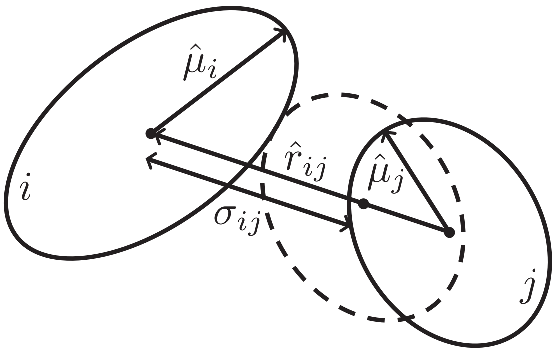

Figure 2.10 Definition of the contact distance σ_{ij} for ellipsoidal particles i and j with unit vectors $\hat{\mu}_i$ and $\hat{\mu}_j$ that characterize the orientations of their major axes. σ_{ij} is the center-to-center separation r_{ij} at which ellipsoidal particles first touch when they are brought together along $\vec{r}_{ij}$ at fixed orientation.

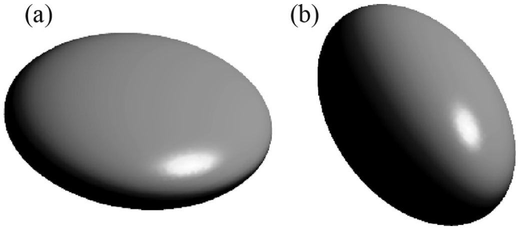

Figure 2.11 (a) Oblate and (b) prolate spheroids with aspect ratios $\alpha = 0.375 < 1$ and $\alpha = 1.7 > 1$.

symmetry is termed an oblate (prolate) spheroid, as shown in Figure 2.11. We will refer to both ellipses and spheroids as ellipsoidal particles and characterize the ratio of the major to minor axes by $\alpha = a/b$ in 2D or the ratio of the polar to equatorial lengths in 3D. As shown in Figure 2.10, configurations of ellipsoidal particles are specified by the centers of mass $\vec{r}_i$ and the orientation of the major axis $\hat{\mu}_i$ of each particle i.

One of the simplest methods for obtaining an approximate expression for the contact distance between ellipsoidal particles is the ‘Gaussian approximation’ introduced by Berne and Pechukas [38]. In this method, the contact distance between two ellipsoidal particles of the *same* size is approximated by finding the overlap between two Gaussian functions, $G_i(\vec{r})$ and $G_j(\vec{r})$, whose contour surfaces at $1/e$ coincide with the surfaces of particles i and j. $G_i(\vec{r}) = e^{-((x-x_i)^2+(y-y_i)^2)/a_i^2-(z-z_i)^2/b_i^2}$ for an ellipsoidal particle centered at (x_i, y_i, z_i) with orientation $\hat{\mu}_i = \hat{z}$ and major (minor) axis a (b). More generally, $G_i(\vec{r}) = e^{-(r-r_i)_k(\gamma^{-1})_{kl}(r-r_i)_l}$, where $\gamma_{kl} = (a^2 - b^2)\mu_k\mu_l + b^2\delta_{kl}$, δ_{kl} is the Kronecker delta, and $k, l \in \{x, y, z\}$. Integrating $\int G_i(\vec{r})G_j(\vec{r})d^3r$, we obtain another Gaussian function, $G_0 e^{-2(r_{ij}/\sigma_{ij}^g)^2}$ [39].

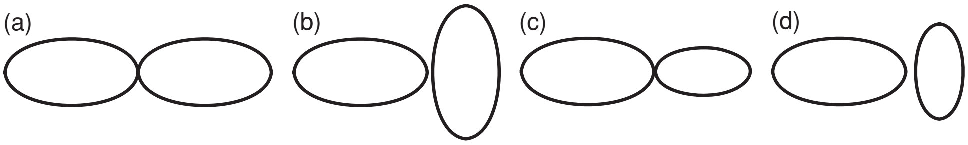

Figure 2.12 Ellipses with $\alpha = 2$ at their 'Gaussian contact distance' σ_{ij}^c. For two ellipses with the same size, (a) the end-to-end configuration is exact, while (b) the side-to-end configuration has a relative error of 5%. For two ellipses with $a_j/a_i = 1.4$, (c) the end-to-end configuration has a relative error of 1%, while (d) the side-to-end configuration has a relative error of 10%.

$\sigma_{ij}^g > \sigma_{ij}$ is an approximation to the true contact distance, and is given by:

$$\sigma_{ij}^g = \frac{\sigma_0}{\sqrt{1 - \frac{\chi}{2}\sum\limits_{\pm}\frac{(\hat{r}_{ij}\cdot\hat{\mu}_i \pm \hat{r}_{ij}\cdot\hat{\mu}_j)^2}{1 \pm \chi\hat{\mu}_i\cdot\hat{\mu}_j}}}, \tag{2.5}$$

where $\chi = (a^2 - b^2)/(b^2 + a^2)$ and $\sigma_0 = b$.

The Gaussian approximation was generalized by Cleaver *et al.* for ellipsoidal particles with different sizes and aspect ratios [40]. This approximation for the contact distance σ_{ij}^c has a similar simple analytic form:

$$\sigma_{ij}^c = \frac{\sigma_0}{\sqrt{1 - \frac{\chi}{2}\sum\limits_{\pm}\frac{(\beta\hat{r}_{ij}\cdot\hat{\mu}_i \pm \beta^{-1}\hat{r}_{ij}\cdot\hat{\mu}_j)^2}{1 \pm \chi\hat{\mu}_i\cdot\hat{\mu}_j}}}, \tag{2.6}$$

where $\sigma_0 = \sqrt{(b_i^2 + b_j^2)/2}$, $\chi = \left(\frac{(a_i^2-b_i^2)(a_j^2-b_j^2)}{(a_j^2+b_i^2)(a_i^2+b_j^2)}\right)^{1/2}$, and $\beta = \left(\frac{(a_i^2-b_i^2)(a_j^2+b_i^2)}{(a_j^2-b_j^2)(a_i^2+b_j^2)}\right)^{1/4}$ in the Cleaver form. The Gaussian approximation to the contact distance behaves poorly for ellipsoidal particles with different sizes. In Figure 2.12, we show σ_{ij}^c for different relative orientations of bidisperse ellipses; the relative deviation from the true contact distance can be as large as $e \sim 10\%$ for $a_j/a_i = 1.4$ and $\alpha = 2.0$. *The Gaussian approximation should therefore not be used to study 2D amorphous ellipse packings since polydispersity is required to suppress bond orientational order.* For monodisperse ellipses with $\alpha = 2.0$, $0\% < e < 5\%$, and similar results are expected for 3D systems.

Perram and Wertheim pursued a related approach, yet their formulation yields the exact contact distance for ellipsoidal particles with different sizes in 2D and 3D [41]. They define $F_i^{\text{single}}(\vec{r}) = (r - r_i)_k(\gamma^{-1})_{kl}(r - r_i)_l$, where $F_i^{\text{single}}(\vec{r}) > 1 (< 1)$ for a point $\vec{r}$ outside (inside) ellipsoidal particle i. They were able to show that for a given λ, the function $F_{ij}^{\text{pair}}(\vec{r}, \lambda) = \lambda F_i^{\text{single}}(\vec{r}) + (1 - \lambda)F_j^{\text{single}}(\vec{r})$ has a unique minimum at $\vec{r} = \vec{r}_{\min}(\lambda)$. Note that $F_{ij}^{\text{pair}}(\vec{r}_{\min}(\lambda), \lambda) = 0$ when $\vec{r}_{\min}(\lambda = 0) = \vec{r}_j$

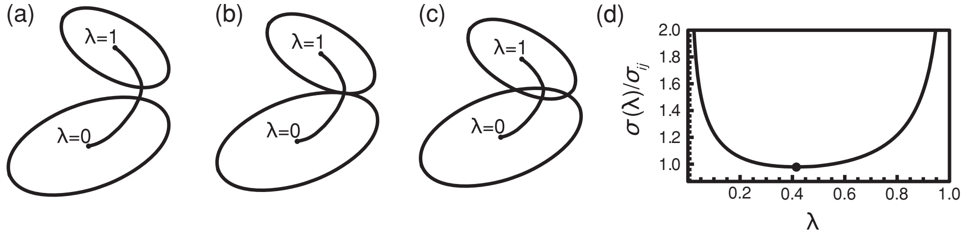

Figure 2.13 Three configurations with the same $\hat{r}_{ij}$, $\hat{\mu}_i$, and $\hat{\mu}_j$, but different r_{ij} are shown in panels (a)–(c). The solid curve $\vec{r}_{\min}(\lambda)$ starts from the center of ellipse j at $\lambda = 0$ and ends at the center of ellipse i at $\lambda = 1$. In (a), $F_{ij} > 1$ for nontouching ellipses; in (b), $F_{ij} = 1$ for 'just-touching' ellipses; and in (c), $F_{ij} < 1$ for overlapping ellipses. σ_{ij} has the same value for (a)–(c). In (d), we show that $\sigma(\lambda)/\sigma_{ij} = [F_{ij}/F_{ij}^{\text{pair}}(\vec{r}_{\min}(\lambda), \lambda)]^{1/2}$ has a minimum at $\lambda^* = 0.415$ (filled circle) for this particular choice of $\hat{r}_{ij}$, $\hat{\mu}_i$, and $\hat{\mu}_j$.

and $\vec{r}_{\min}(\lambda = 1) = \vec{r}_i$. Thus, λ parameterizes a curve $\vec{r}_{\min}(\lambda)$ for which the function $F_{ij}^{\text{pair}}(\vec{r}_{\min}(\lambda), \lambda))$ goes from 0 at $\lambda = 0$ back to 0 at $\lambda = 1$ and is concave down for λ in the range [0, 1] [41].

For the nonoverlapping ellipsoidal particles i and j in Figure 2.13(a), $F^{\text{single}}(\vec{r}_{\min}(\lambda), \lambda) > 1$ for both i and j over some range of λ, which implies that $F_{ij}^{\text{pair}}(\vec{r}_{\min}(\lambda), \lambda) > 1$ for the same range of λ. For the overlapping ellipsoidal particles in Figure 2.13(c), $F^{\text{single}}(\vec{r}_{\min}(\lambda), \lambda) < 1$ for either ellipses i or j for all λ, and thus $F_{ij}^{\text{pair}}(\vec{r}_{\min}(\lambda), \lambda) < 1$ for all λ [41]. Since the maximum over λ of $F_{ij}^{\text{pair}}(\vec{r}_{\min}(\lambda), \lambda) < 1$ for overlapping ellipsoidal particles and is greater than unity for nonoverlapping ellipsoidal particles, the two particles will come into contact when $F_{ij} \equiv \max_\lambda F_{ij}^{\text{pair}}(\vec{r}_{\min}(\lambda), \lambda) = 1$. Perram and Wertheim further showed that $F_{ij} = (r_{ij}/\sigma_{ij})^2$, where the contact distance $\sigma_{ij} = \min_\lambda \sigma(\lambda)$ and $\sigma(\lambda) = \sigma_{ij}^c$ with λ-dependent parameters $\sigma_0(\lambda) = \frac{1}{2}\sqrt{\frac{b_i^2}{\lambda} + \frac{b_j^2}{1-\lambda}}$, $\chi(\lambda) = \left(\frac{(a_i^2-b_i^2)(a_j^2-b_j^2)}{(a_j^2+\frac{1-\lambda}{\lambda}b_i^2)(a_i^2+\frac{\lambda}{1-\lambda}b_j^2)}\right)^{1/2}$, and $\beta(\lambda) = \left(\frac{(a_i^2-b_i^2)(a_j^2+\frac{1-\lambda}{\lambda}b_i^2)}{(a_j^2-b_j^2)(a_i^2+\frac{\lambda}{1-\lambda}b_j^2)}\right)^{1/4}$. We obtain the Cleaver Gaussian approximation for σ_{ij}, if instead of minimizing $\sigma(\lambda)$ over λ, we set $\lambda = 1/2$ [42, 40].

The final step in determining the contact distance is to calculate $\lambda_{\min}$ at which $\sigma(\lambda)$ is a minimum. This task can be approached in two ways: either minimize $\sigma(\lambda)$ numerically or derive an analytical expression for $\lambda_{\min}$. We prefer the latter because it improves the efficiency and accuracy of the calculation. Determining $\lambda_{\min}$ involves solving a quartic (for 2D bidisperse ellipses) or quintic (for 3D monodisperse ellipsoids) polynomial equation.

We now sketch an outline for deriving these polynomial equations since this has not yet appeared in the literature. First, minimizing $\sigma(\lambda)$ with respect to λ is the same as maximizing $\sigma^{-2}(\lambda)$ over λ. We then make the substitution $y = \lambda - 1/2$ (because it simplifies the algebra) and define $h(y) = [\sigma(y + 1/2)]^{-2}$. Thus, to find

$\lambda_{\min}$, we must solve $dh(y)/dy = f(y)/g(y) = 0$ for $y_{\min}$, where $f(y)$ and $g(y)$ are polynomials, by solving for the roots of $f(y)$. For 2D bidisperse ellipses (3D monodisperse ellipsoids), $f_{2D}(y)$ ($f_{3D}(y)$) is a quartic (quintic) polynomial with coefficients that depend on four parameters J, K, L, and M:

$$f_{2D}(y) = q_4 y^4 + q_3 y^3 + q_2 y^2 + q_1 y + q_0 \tag{2.7}$$

$$q_0 = \frac{1}{16} J(L+4) - \frac{1}{16} K(J+4) \tag{2.8}$$

$$q_1 = -(1 + K/2)(J+2) \tag{2.9}$$

$$q_2 = -\frac{1}{2} J(L+6) - \frac{1}{2} K(3J+2) \tag{2.10}$$

$$q_3 = -2JK \tag{2.11}$$

$$q_4 = J(L-K) \tag{2.12}$$

$$J = \frac{a_j^2 - (a_j^2 - b_j^2)(\hat{r}_{ij} \cdot \hat{\mu}_j)^2}{a_i^2 - (a_i^2 - b_i^2)(\hat{r}_{ij} \cdot \hat{\mu}_i)^2} - 1 \tag{2.13}$$

$$K = \left(\frac{a_j b_j}{a_i b_i} \right)^2 - 1 \tag{2.14}$$

$$L = \frac{1}{a_i^2 b_i^2} (a_i^2 a_j^2 + b_i^2 b_j^2 + (a_i^2 - b_i^2)(a_j^2 - b_j^2)(\hat{\mu}_i \cdot \hat{\mu}_j)^2) - 2 \tag{2.15}$$

$$f_{3D}(y) = q_5 y^5 + q_4 y^4 + q_3 y^3 + q_2 y^2 + q_1 y + q_0 \tag{2.16}$$

$$q_0 = \frac{1}{16} J(L+4) \tag{2.17}$$

$$q_1 = -(J+2) + \frac{1}{8} M(L+8) \tag{2.18}$$

$$q_2 = -\frac{1}{2} J(L+6) \tag{2.19}$$

$$q_3 = -M(L+4) \tag{2.20}$$

$$q_4 = JL \tag{2.21}$$

$$q_5 = 2ML \tag{2.22}$$

$$J = \frac{\alpha^2 - 1}{\alpha^2} \frac{((\hat{r}_{ij} \cdot \hat{\mu}_i)^2 - (\hat{r}_{ij} \cdot \hat{\mu}_j)^2)}{1 - \frac{\alpha^2 - 1}{\alpha^2} (\hat{r}_{ij} \cdot \hat{\mu}_i)^2} \tag{2.23}$$

$$L = \frac{(\alpha^2 - 1)^2}{\alpha^2} (1 - (\hat{\mu}_i \cdot \hat{\mu}_j)^2) \tag{2.24}$$

$$\begin{aligned} M = {} & \frac{(\alpha^2 - 1)^2}{\alpha^2} \frac{1}{1 - \frac{\alpha^2 - 1}{\alpha^2} (\hat{r}_{ij} \cdot \hat{\mu_i})^2} ((\hat{r}_{ij} \cdot \hat{\mu_i})^2 + (\hat{r}_{ij} \cdot \hat{\mu_j})^2 \\ & - \hat{\mu}_i \cdot \hat{\mu_j} (2(\hat{r}_{ij} \cdot \hat{\mu_i})(\hat{r}_{ij} \cdot \hat{\mu_j}) - \hat{\mu}_i \cdot \hat{\mu}_j) - 1). \end{aligned} \tag{2.25}$$

Table 2.1 *The base 10 logarithm of the relative error of the Gaussian, linear, and quadratic approximations for the contact distance from the exact value,* $\log_{10}(|\sigma_{\text{approx}} - \sigma_{\text{exact}}|/\sigma_{\text{exact}})$*, for bidisperse ellipses with size ratio 1.4 over a range of aspect ratios* α*. These estimates were averaged over* $\hat{r}_{ij}$ *and orientations.*

Approximation	$\alpha = 1.0$	1.2	1.5	2.0	3.0	10.0
Gaussian	−2.0	−2.0	−1.9	−1.6	−1.3	−0.4
Linear	−3.9	−3.8	−3.7	−3.6	−1.5	−0.1
Quadratic	−6.3	−6.2	−6.3	−5.0	−3.8	−1.4

The coefficients J, K, L, and M reveal the symmetry of the polynomial $f(y)$. $M = 0$ in two dimensions, $L = 0$ when ellipsoidal particles i and j of the same aspect ratio have parallel orientations, $K = 0$ when i and j have the same size, and $J = 0$ when the orientations of ellipsoids i and j of the same size and aspect ratio have the same angle with respect to their center-to-center vector $\vec{r}_{ij}$. The symmetries found for M, L, and K are obvious (2D, parallel, and same size), but the symmetry found in J is not. When $J = 0$, $f_{3D}(y)$ only contains odd terms in y, which implies that $\lambda_{\text{min}} = 1/2$ is a solution, and we have a simple expression for the contact distance in a nontrivial case!

We are now in a position to quantitatively compare the exact results for the contact distance to various levels of approximation. For example, we can truncate $f(y)$ at either linear or quadratic order, which yield:

$$\lambda_{\text{min}}^{\text{linear}} = -\frac{q_0}{q_1}; \quad \lambda_{\text{min}}^{\text{quadratic}} = -\frac{\left(q_1 - \sqrt{q_1^2 - 4q_0q_2}\right)}{2q_2}. \tag{2.26}$$

Even at this level of approximation, the solution is significantly more precise than the commonly used Gaussian approximation, and is more efficient than numerically solving a quartic or quintic equation at each step in the packing-generation process. To demonstrate the improved precision, we include Table 2.1 that lists the relative error in finding the true contact distance for the Gaussian, linear, and quadratic approximation methods for two ellipses i and j with $a_j/a_i = 1.4$ over a range in aspect ratios from $\alpha = 1$ to 10. These estimates were averaged over $\hat{r}_{ij}$ and orientations.

2.3.3 Particle shape annealing

Static packings of anisotropic particles can also be generated using a ‘particle shape annealing’ method. This method involves starting with a static packing of spherical particles, changing a shape parameter at a given rate to cause the particles to become

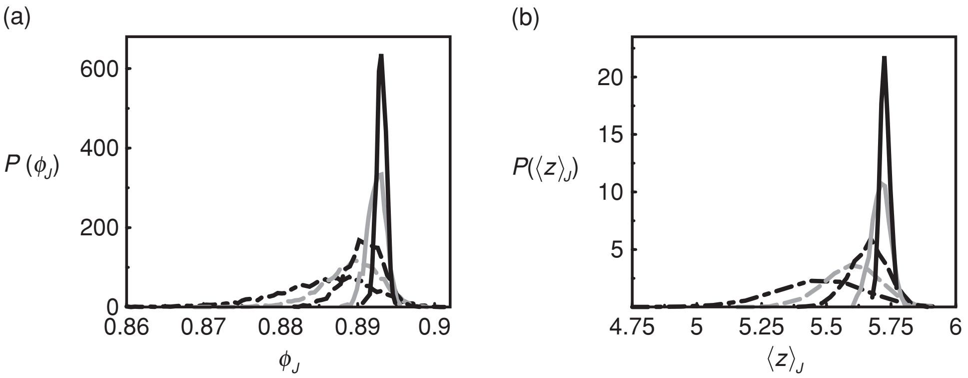

Figure 2.14 Distribution of (a) packing fractions ϕ_J and (b) mean contact numbers $\langle z\rangle_J$ at jamming onset for ellipses at $\alpha = 1.6$ using the isotropic compression packing-generation method as a function of system size $N = 32$ (black dot dashed), 64 (gray dashed), 256 (black dashed), 512 (gray solid), and 1024 (black solid).

nonspherical, and using the compression method described in Section 2.1 to obtain a packing of just-touching particles with the new shape parameter.

We provide specific details of the particle shape annealing method for creating packings of ellipsoidal particles at a given aspect ratio α. The process starts with a static packing of spherical particles. The aspect ratio of each disk/sphere is then increased from $\alpha = 1$ to $1 + \Delta\alpha$ with the direction of the major axis chosen randomly. A static packing of ellipsoidal particles at $\alpha = 1 + \Delta\alpha$ is formed from this initial state using the compression method from Section 2.1. The ellipsoidal particles in this new packing are further elongated, and the protocol is repeated until a packing with the desired aspect ratio is reached. From our previous studies of ellipse packings [33], we find that the average jammed packing fraction $\langle\phi_J\rangle$ is larger than that obtained using the isotropic compression method, even though the packings do not possess increased spatial or orientational order as shown in Figure 2.18(b). In addition, the particle shape annealing procedure does not depend sensitively on the step size $\Delta\alpha$, at least for sufficiently small $\Delta\alpha$.

2.4 Distributions of jamming onsets

In previous sections, we described several methods for generating jammed particle packings. By creating packings for large numbers of independent, random initial conditions, we can create an ensemble of static packings and measure the distribution of jammed packing fractions $P(\phi_J)$ as shown in Figure 2.14(a) for ellipses at $\alpha = 1.6$ and several system sizes from $N = 32$ to 1024. Note that the distribution is broad for small systems, but approaches a δ-function in the large-N limit.

Packing-generation procedures for frictionless spherical and nonspherical grains give rise to jammed packings with well-defined mean packing fractions $\langle \phi_J \rangle$ in the large-system limit. In previous studies, we found that the width $\mathcal{W}$ of the packing fraction distribution for spherical particles scaled as $\mathcal{W} \sim N^{-\nu}$, with $\nu \approx 0.5$ [13]. Preliminary studies indicate that the scaling exponent depends on the aspect ratio α for ellipsoidal particles [43].

3 Mechanical stability

After static particle packings are generated, we can test to determine whether they are *mechanically stable*, i.e. in a state of total force and torque balance for each particle (except floater particles that are not locally stable) and stable with respect to infinitesimal deformations. Mechanical stability can be assessed by calculating the dynamical matrix of second derivatives of the total potential energy V [11]:

$$M_{kl} = \frac{\partial^2 V}{\partial \vec{\xi}_k \partial \vec{\xi}_l}, \tag{2.27}$$

where $\vec{\xi}_k$ are the relevant configurational degrees of freedom for particle k. As examples, $\vec{\xi}_k = \{x_k, y_k\}$ for disks and $\vec{\xi}_k = \{x_k, y_k, d_k\theta_k\}$ for ellipses, where x_k and y_k are the center of mass coordinates, θ_k is the angle between the major axis and $\hat{x}$, and d_k is a lengthscale for dimensional consistency that is typically obtained from the second moment of the mass distribution of the grain about its major axis. For ellipses, $d_k = \frac{1}{4}\sqrt{a_k^2 + b_k^2}$. In this discussion, we will assume that all grains have mass $m = 1$ with a uniform mass distribution. The dimension of the dynamical matrix is determined by the number of degrees of freedom (DOF) $d_f\mathcal{N}$ for a given system, where $\mathcal{N} = N - N_f$ and N_f is the number of floaters in the system. For example, $d_f = 2$ (3) for disks (ellipses). The dynamical matrix is real and symmetric with dimension $d_f\mathcal{N} \times d_f\mathcal{N}$.

To determine whether or not a static packing is mechanically stable, we diagonalize M_{kl} to find its $d_f\mathcal{N}$ eigenvalues e_i and associated eigenvectors $\hat{e}_i$, with $\hat{e}_i^2 = 1$. For systems with periodic boundary conditions, d of these eigenvalues are zero due to translational invariance. For mechanically stable states, the dynamical matrix possesses $d_f\mathcal{N} - d$ nontrivial eigenvalues with $e_i > 0$. This implies that all nontrivial deformations give rise to particle overlap and an increase in the potential energy to second order. In practice, we typically use a threshold (e.g. $e_{\min} = 10^{-6}$) above which eigenvalues are deemed nonzero [28].

To illustrate the importance of testing mechanical stability, we show two $N = 7$ monodisperse static disk packings (solid circles) in Figures 2.15(a) and (b) at nearly the same packing fraction $\phi \approx 0.73$. The packing in (a) is mechanically stable,

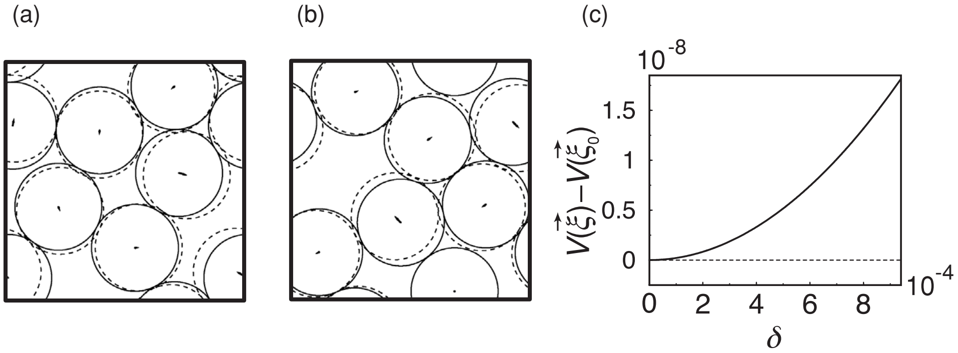

Figure 2.15 (a) Mechanically and (b) locally stable packings at nearly identical packing fractions. The original (perturbed) packings are shown using solid (dashed) circles. The packings are deformed according to: $\vec{\xi} = \vec{\xi}_0 + \delta \hat{e}_1$, where $\vec{\xi}_0$ is the unperturbed configuration, δ is the amplitude of the perturbation, and $\hat{e}_1$ is the eigenvector of the dynamical matrix (evaluated at $\vec{\xi}_0$) corresponding to the lowest nontrivial eigenvalue. Solid lines connecting the centers of corresponding particles in configurations $\vec{\xi}$ and $\vec{\xi}_0$ at $\delta = 0.2$ are also shown. (c) Change in potential energy per particle $V(\vec{\xi}) - V(\vec{\xi}_0)$ versus δ for the (a) mechanically stable (solid line) and (b) locally stable (dashed line) configurations. Note that the locally stable configuration can be deformed along $\hat{e}_1$ without energy cost.

while that in (b) is only locally stable [44]. To show this, we diagonalized the dynamical matrix for these configurations and then deformed them by δ along the eigenvector $\hat{e}_1$ corresponding to the smallest nontrivial eigenvalue: $\vec{\xi} = \vec{\xi}_0 + \delta \hat{e}_1$. In Figure 2.15(c), we plot the change in energy $\Delta V \equiv V(\vec{\xi}) - V(\vec{\xi}_0)$ versus δ. $\Delta V \sim \delta^2$ for the mechanically stable packing, while $\Delta V = 0$ for the locally stable packing. In Figure 2.15(b), we can see that for locally stable packings there are collective modes that do not give rise to particle overlap and thus do not change the potential energy.

The spectrum of normal modes (or vibrational frequencies) $\omega_i = \sqrt{e_i/M}$, where $M = Nm$, yields significant insight into the structural and mechanical properties of MS packings. The normal mode spectra are typically visualized in two ways: (1) the ordered list of $d_f \mathcal{N} - d$ nonzero frequencies and (2) the density of states (DOS) $D(\omega) = (N(\omega + \delta\omega) - N(\omega))/\delta\omega$, where $N(\omega)$ is the number of modes with frequency ω. The spectrum of normal modes for jammed bidisperse disk packings is shown in Figure 2.16, where we plot the sorted list of frequencies and DOS in (a) and (b), respectively. For jammed disk packings, we see the characteristic continuous increase in the sorted frequencies in (a) and plateau in the DOS at low frequencies in (b) [13]. In contrast to jammed sphere packings, we find three distinct regimes, separated by two gaps, in the normal mode spectrum for jammed ellipse packings over a range of aspect ratios [33], [37] as shown in

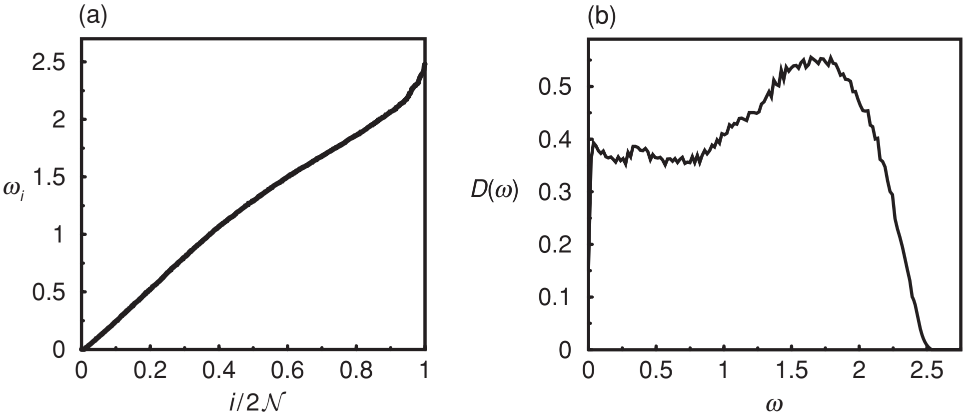

Figure 2.16 (a) Vibrational modes ω_i sorted in increasing order versus index $i/2\mathcal{N}$ normalized by the number of DOF and (b) density of vibrational modes $D(\omega)$ (averaged over 100 configurations) for jammed 50–50 bidisperse disk packings with diameter ratio $d = 1.4$ at $\phi - \phi_J = 10^{-4}$.

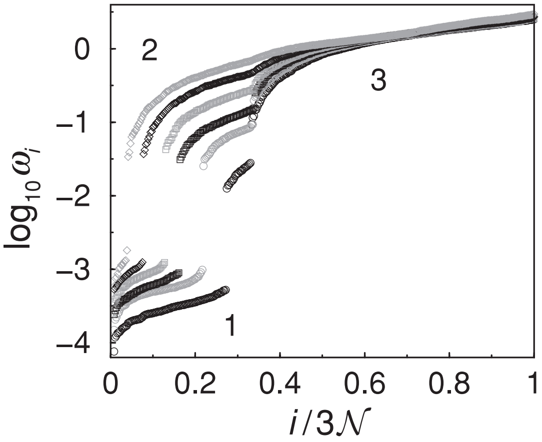

Figure 2.17 Normal mode frequencies ω_i vs. index $i/3\mathcal{N}$ normalized by the number of DOF, sorted by increasing frequency for $N = 120$ ellipse packings at six aspect ratios, $\alpha = 1.02$ (black circles), 1.06 (gray circles), 1.1 (black squares), 1.2 (gray squares), 1.4 (black diamonds), and 1.8 (gray diamonds). The sorted frequency spectrum possesses three distinct branches (numbered 1, 2, and 3). Adapted from reference [33].

Figure 2.17. A novel feature of ellipse packings is that in the just-touching limit perturbations along modes in region 1 give rise to *quartic*, not quadratic, increases in potential energy. Moreover, modes in regions 1 and 2 are primarily rotational in character.

4 Measurements of structural and mechanical properties

In previous sections, we discussed methods to generate mechanically stable particle packings. In this section, we will describe a number of measurements that can be performed to quantify the structural and mechanical properties of these jammed packings, which include the contact number, pair distribution function, structure factor, bond orientational and nematic order parameters, positional correlation functions, and elastic moduli. The focus will be on methodology, not a comprehensive discussion of the results for jammed particle packings. That is, the purpose of this section is to facilitate the calculation of these quantities for jammed particle packings.

4.1 Contact number

In a static granular packing, mechanical stability (to second order) can be achieved only if the number of contacts is greater than or equal to the number of degrees of freedom (DOF), $N_c \geq \mathcal{N} d_f - d + 1$ [45], [46]. We subtract off d trivial DOF due to translational invariance in systems with periodic boundary conditions and add 1 from the packing fraction DOF. For N frictionless spherical grains in d dimensions, jammed packings are *isostatic* [47], [48] with $N_c = \mathcal{N} d - d + 1$. Using $N_c = \mathcal{N}\langle z\rangle/2$, we obtain $\langle z\rangle_{\mathrm{iso}} = 2d - (d-1)/\mathcal{N}$ for frictionless packings of spherical particles. In the large-$\mathcal{N}$ limit, $\langle z\rangle_{\mathrm{iso}} = 2d$ as shown in Figure 2.18(a) for $\alpha = 1$.

When counting the number of contacts in jammed systems, we must first remove all floaters in the system since they do not contribute to the force network. We assume that particles are floaters if they are not locally stable. Convex particles must generally have at least $d_f + 1$ contacts to remain locally stable. Thus, disks must have at least three contacting neighbors; ellipses, 2D n-mers, and spheres must have at least four contacting neighbors; and ellipsoids and 3D n-mers must have at least six contacting neighbors. However, counter-examples include a disk with three contacting neighbors on one side of its equator and an ellipse with three contacts, whose normals at the points of contact intersect at a single point [16] as shown in Figure 2.19.

Once all floaters have been removed, N_c is obtained by counting the number of just-touching (slightly overlapped) pairs of particles. Since there are two contacting particles for each contact, the average number of contacts per particle $\langle z\rangle = 2N_c/\mathcal{N}$. Note that the constraint of mechanical stability is global, i.e. on N_c or $\mathcal{N}\langle z\rangle/2$, not the contact numbers of individual grains z_i. We show the distribution of z_i for bidisperse disk packings in Figure 2.20. Note that a large fraction of particles have three (and five) contacts, not four.

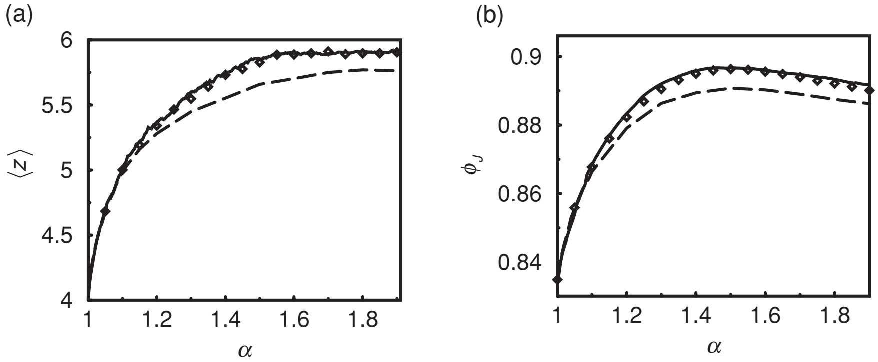

Figure 2.18 Average (a) contact number $\langle z \rangle$ and (b) packing fraction at jamming ϕ_J versus aspect ratio α for bidisperse ellipse packings using the isotropic compression (dashed line) and particle shape annealing methods. Two annealing rates are shown, $\Delta\alpha = 0.05$ (solid line) and 0.005 (diamonds). Adapted from reference [33].

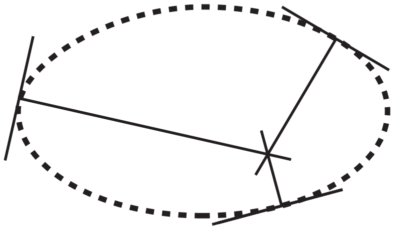

Figure 2.19 Ellipses are generically locally jammed, i.e. the ellipse can neither translate nor rotate without causing particle overlap with other particles held fixed, when they possess four or more contacts. However, ellipses can be locally jammed with three contacts if the normals to the tangent lines at contact happen to intersect at a single point [16].

Unlike spherical particles, ellipsoidal particles are *hypostatic* with $N_c < \mathcal{N} d_f - d + 1$. Packings of ellipsoidal particles can have nearly any value of contact number from the isostatic value for spherical particles $\langle z \rangle_{\text{iso}} = 2d$ to the isostatic value for ellipsoidal particles $\langle z \rangle_{\text{iso}} = 2d_f$. In Figure 2.18(a), we show that $\langle z \rangle$ ranges from $\langle z \rangle = 4$ when $\alpha = 1$ to $\langle z \rangle \lesssim 6$ (for particle shape annealing) near $\alpha = 2$ for ellipse packings [16], [33], [37].

4.2 Pair distribution function and structure factor

The pair distribution function $g(\vec{r})$ gives the probability for finding two particles $\vec{r}$ apart in a given system normalized by the probability for finding two particles separated by $\vec{r}$ in an ideal gas at the same density. In isotropic systems, the pair distribution function only depends on separation r. Here, $g(r)$ can be used to detect

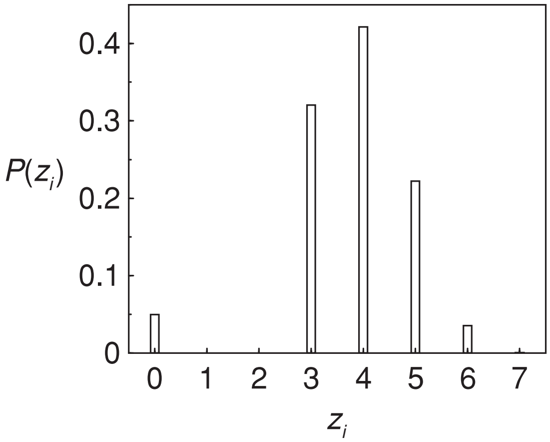

Figure 2.20 Histogram of the number contacts for individual particles z_i for jammed packings of bidisperse disks. Note that there are significant fluctuations away from four contacts, but all particles have $z_i \geq 3$ except for floaters.

whether systems exist in the gas, liquid, or solid phases, and provide a sensitive measure of the distance to jamming in particle packings. $g(r)$ can be expressed as:

$$g(\vec{r}) = \frac{V}{N^2}\left\langle \sum_{i=1}^{N}\sum_{i\neq j}^{N} \delta(\vec{r}-\vec{r}_{ij})\right\rangle, \tag{2.28}$$

where V is the volume of the system [27]. In simulations, the δ-function is replaced by a function that is nonzero over a small range δr. Also, in periodic systems with simulation cell size $\mathcal{L}$, the maximum separation is $\mathcal{L}/\sqrt{2}$; however, the statistics are greatly reduced for $r > \mathcal{L}/2$. In liquids and solids, $g(r)$ is a function ϕ and T, but in model hard sphere systems, $g(r)$ is only a function ϕ.

The pair distribution function has strikingly different features for fluids, jammed packings, and crystalline systems as shown in Figure 2.21. Note that we normalize r by the rms contact distance $\langle\sigma^2\rangle^{1/2}$ averaged over all particle species to account for polydispersity and anisotropic particles. For monodisperse systems, $\langle\sigma^2\rangle^{1/2}$ is the particle diameter. For fluids (Figure 2.21(a)) with only short-range correlations, $g(r)$ has noticeable first and second neighbor peaks and then decays to 1 beyond 3–4 particle diameters.

For crystalline solids, $g(r)$ possesses sharp peaks that correspond to the different interparticle distances allowed by the symmetry of the lattice. In Figure 2.21(c), we show $g(r)$ for a hexagonal crystal in 2D. The hexagonal lattice is composed of linear combinations of the vectors $\hat{n}_1 = (1,0)$ and $\hat{n}_2 = (1/2, \sqrt{3}/2)$. In units of the particle diameter, the lattice vectors are $\vec{n}_{kl} = k\hat{n}_1 + l\hat{n}_2$, where k, l are nonnegative integers, and the corresponding distances

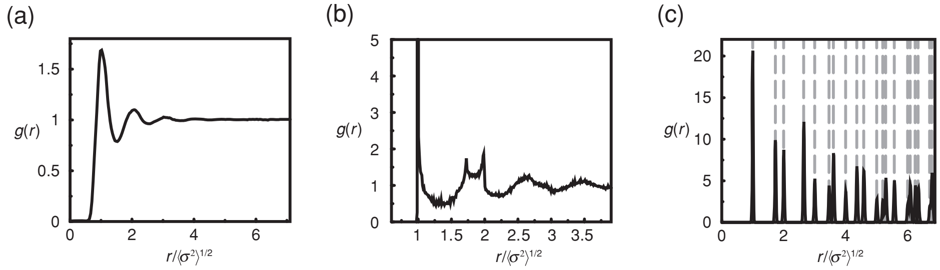

Figure 2.21 Pair distribution function, $g(r)$, for (a) liquid (b) jammed, and (c) crystalline systems. In (a), we show $g(r)$ for a 2D bidisperse system at $\phi = 0.7$ and temperature $T/\epsilon = 0.004 \gg T_g$ (where $k_b = 1$ and T_g is the glass transition) with repulsive linear spring interactions. In (b) (adapted from reference [13]), we show $g(r)$ for jammed 3D monodisperse packings at $\phi - \phi_J = 10^{-2}$ using the repulsive linear spring potential. Note that the first peak in (b) extends to $g(r \to \sigma) \approx 40$. $g(r)$ for a hexagonal crystal in 2D near $\phi_{\text{hex}} = \pi/2\sqrt{3}$ and $T = 0$ is plotted in (c). The dashed vertical lines indicate the possible separations for the hexagonal lattice.

are $n_{kl} = \sqrt{k^2 + lk + l^2} = 1, \sqrt{3}, 2, \sqrt{7}, 3, 2\sqrt{3}, \sqrt{13}, \ldots$. A similar procedure can be followed for other crystals, e.g. the face centered cubic (FCC) lattice, with $\hat{n}_1 = (1, 0, 0)$, $\hat{n}_2 = (1/2, \sqrt{3}/2, 0)$, and $\hat{n}_3 = (1/2, 1/2\sqrt{3}, \sqrt{2/3})$, and $n_{klm} = \sqrt{k^2 + l^2 + m^2 + kl + lm + km} = 1, \sqrt{3}, 2, \sqrt{6}, \sqrt{7}, \ldots$.

Even though $g(r)$ for glassy systems does not show strong signatures that signal the glass transition [49], there are several key features of $g(r)$ that signal the onset of jamming. For example, as systems approach the jamming transition, the height of the first peak diverges as its width tends to zero and the broad second peak found in liquids splits into two peaks, both of which become singular near jamming [13], [50]. In Figure 2.21(b), we show these features for a 3D monodisperse system with $\phi - \phi_J = 10^{-2}$.

The pair distribution function can be measured easily in granular and colloidal systems via direct visualization of particles. On smaller lengthscales or in cases where direct visualization is not possible, we can obtain structural information, such as the structure factor $S(\vec{k})$ from light or x-ray scattering. $S(\vec{k})$ is the autocorrelation function of Fourier transformed density $\rho(\vec{k}) = \sum_{i=1}^{N} e^{\imath \vec{k}\cdot\vec{r}_i}$, $S(\vec{k}) = N^{-1}\langle \rho(\vec{k})\rho(-\vec{k})\rangle$, which can be written as:

$$S(\vec{k}) = \frac{1}{N}\left\langle \sum_{i=1}^{N}\sum_{i\neq j}^{N} e^{\imath \vec{k}\cdot(\vec{r}_i - \vec{r}_j)} \right\rangle, \tag{2.29}$$

where $\vec{k} = (2\pi/\mathcal{L})(n_x\hat{x} + n_y\hat{y} + n_z\hat{z})$, with $n_x, n_y, n_z = 0, 1, \ldots$, are the allowed wavevectors and angle brackets denote an ensemble average. The isotropic $S(k)$

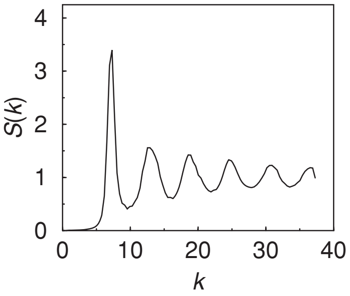

Figure 2.22 Angular averaged structure factor $S(k)$ for jammed monodisperse sphere packings at $\phi - \phi_J = 10^{-4}$. Adapted from reference [13].

can be obtained by angular averaging over $\vec{k}/k$ at fixed k. $S(k)$ is also related to the spatial Fourier transform of $g(r)$, but since simulations have access to particle positions, both are typically calculated directly. In Figure 2.22, we show $S(k)$ for jammed packings of monodisperse spheres at $\phi - \phi_J = 10^{-4}$. A key feature of $S(k)$ for jammed packings is the long-lived fluctuations that occur at $k_n^* = 2\pi n/a$, where $n = 1, 2, 3, \ldots$ and a is the particle diameter, which are a direct result of the divergent first peak in $g(r)$. Recent studies have also investigated the novel power-law scaling of $S(k)$ at low k in jammed sphere packings [51].

4.3 Order parameters

It is important to characterize the translational and orientational order as systems approach the jamming transition. For example, in granular shear flows we must distinguish between crystallization kinetics and jamming behavior [52], [53]. Order parameters that identify various symmetries can be measured and used to quantify order or disorder. We will discuss three commonly used order parameters: the nematic order parameter P_2, which evaluates to one in the case that all orientations of uniaxial particles are parallel; the bond orientational parameter Q_6, which evaluates to one for systems in which the positional degrees of freedom have perfect six-fold symmetry; and a translation order parameter $\mathcal{G}$, which is the ratio of the first minimum to the first maximum in $g(r)$ and tends to zero as systems crystallize.

The nematic order parameter is defined as $P_2 = \langle 2\cos^2\theta - \frac{1}{2}\rangle$ in 2D and $P_2 = \langle \frac{3}{2}\cos^2\theta - \frac{1}{2}\rangle$ in 3D, where angle brackets denote an average over all particles in the system, θ is the angle of the particle director (i.e. the unit vector along the long axis, $\hat{n}$) relative to the average nematic director $\hat{N}$. $\hat{N}$ can be obtained by calculating $\langle \hat{n}\rangle$ or by maximizing P_2 with respect to $\hat{n}$. $P_2 = 1$ for completely aligned systems, whereas $P_2 \sim 1/\sqrt{N}$ $(1/\sqrt{N_d})$ in the absence (presence) of nematic domains, where N_d is the number of domains. In Figure 2.23(c) and (d) we show

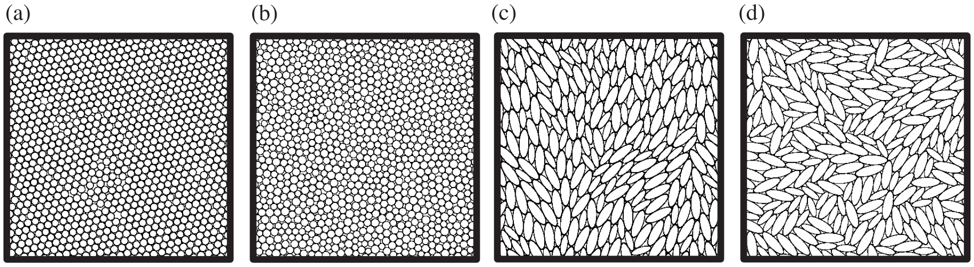

Figure 2.23 Packings that display varying degrees of bond orientational Q_6 and nematic P_2 order. In (a) and (b), we show $N = 1024$ disk packings with polydispersity $p = 1.1$ (1.4), $Q_6^g = 0.93$ (0.03), and $Q_6^l = 0.95$ (0.63). In (c) and (d), we show $N = 256$ monodisperse ellipse packings with $\alpha = 3$ and $P_2 = 0.64$ (0.11) using two different packing protocols.

monodisperse ellipse packings at aspect ratio $\alpha = 3$ and roughly the same packing fraction that were created using two different packing-generation methods. The method used in (c) produces roughly aligned ellipses with $P_2 = 0.64$, while the method in (d) produces randomly oriented ellipses with $P_2 = 0.11$.

The bond orientational order parameter Q_6, which measures hexagonal registry of nearest neighbors, can be calculated "locally," which does not consider phase information, or "globally," which allows phase cancellations. A polycrystal will yield a large value for the local bond orientational order parameter Q_6^l, even though the global order parameter $Q_6^l \sim 1/\sqrt{N_d}$, where N_d is the number of polycrystalline domains. The expressions for the global and local definitions of Q_6 are given below. Equations (2.30) (global), (2.31) (local), (2.32) (global), and (2.33) (local) provide expressions for the bond orientational order parameters in 2D and 3D, respectively:

$$Q_6^g = \frac{1}{N}\left|\sum_{i=1}^{N}\frac{1}{n_i}\sum_{j=1}^{n_i} e^{6\iota\theta_{ij}}\right| \tag{2.30}$$

$$Q_6^l = \frac{1}{N}\sum_{i=1}^{N}\frac{1}{n_i}\left|\sum_{j=1}^{n_i} e^{6\iota\theta_{ij}}\right| \tag{2.31}$$

$$Q_6^g = \left(\frac{4\pi}{13}\sum_{m=-6}^{6}\left|\frac{1}{N}\sum_{i=1}^{N}\frac{1}{n_i}\sum_{j=1}^{n_i} Y_6^m(\theta_{ij}, \phi_{ij})\right|^2\right)^{1/2} \tag{2.32}$$

$$Q_6^l = \left(\frac{4\pi}{13}\sum_{m=-6}^{6}\frac{1}{N}\sum_{i=1}^{N}\frac{1}{n_i}\left|\sum_{j=1}^{n_i} Y_6^m(\theta_{ij}, \phi_{ij})\right|^2\right)^{1/2}, \tag{2.33}$$

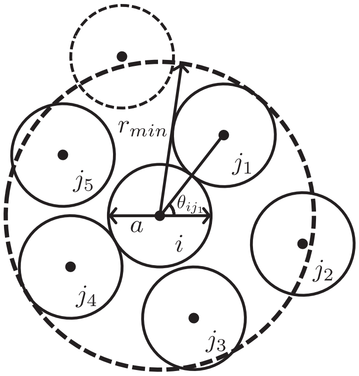

Figure 2.24 The nearest-neighbor range employed for calculations of Q_6. The dashed particle is outside the nearest-neighbor radius $r_{\min}$, which is defined as the first minimum of $g(r)$.

where θ_{ij} is the angle (axial angle in 3D) between a central particle i and neighbors j, ϕ_{ij} is the polar angle between i and j, Y_m^l are the spherical harmonics, and n_i denotes the number of nearest neighbors of i. Two particles are deemed nearest neighbors if their center-to-center separation $r_{ij} < r_{\min}$, which we set as the first minimum of $g(r)$ as shown in Figure 2.24. The spherical harmonics $Y_l^m(\theta_{ij}, \phi_{ij}) = \sqrt{\frac{2l+1}{4\pi}\frac{(l-6)!}{(l+6)!}} e^{\imath m\phi_{ij}} P_l^m(\cos\theta_{ij})$, where $P_l^m(\cos\theta_{ij})$ are Legendre polynomials [54].

In Figure 2.23 we show two jammed disk packings with different polydispersities at roughly the same packing fraction. The lower polydispersity $p = 1.1$ is polycrystalline with a large Q_6^g, while the packing at $p = 1.4$ is amorphous with a negligible Q_6^g. This shows that weakly polydisperse disk packings are prone to crystallization. In Figure 2.25, we show that both finite aspect ratio α and polydispersity p give rise to disorder. $\alpha > 1.2$ and $p > 1.2$ both lead to amorphous packings with small Q_6^g. In Figure 2.26, we show snapshots of dimer packings as a function of increasing α and disorder. Panels (a)–(f) correspond to the dashed line in Figure 2.25.

We also mention briefly the order parameter $\mathcal{G} = g(r_{\min})/g(r_{\max})$ that is sensitive to translational order. It is zero for crystalline systems, but is a finite constant for jammed systems. It has been used for example in studies of metallic and structural glasses to determine the onset of crystallization as a function of cooling rate [55].

4.4 Correlation functions and lengths

Although jammed systems are amorphous on macroscopic scales, they can possess order over short lengthscales that is averaged out when calculating global order parameters such as Q_6 and P_2. For instance, jammed systems of monodisperse disks

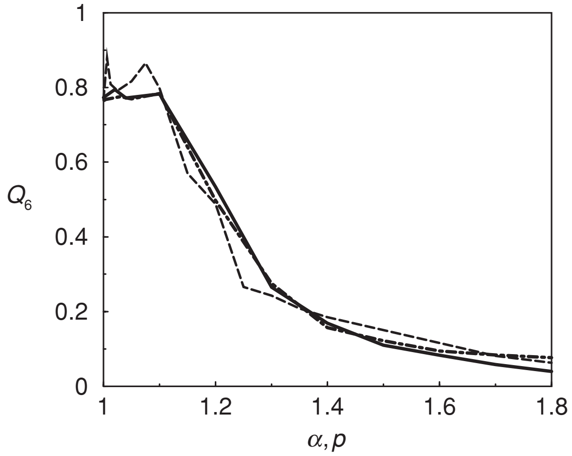

Figure 2.25 Q_6 (global) versus aspect ratio α for monodisperse ellipse packings (solid line), α for 2D dimer packings (dashed line), and polydispersity p for disk packings (dot-dashed line). All data are for $N = 256$ particles.

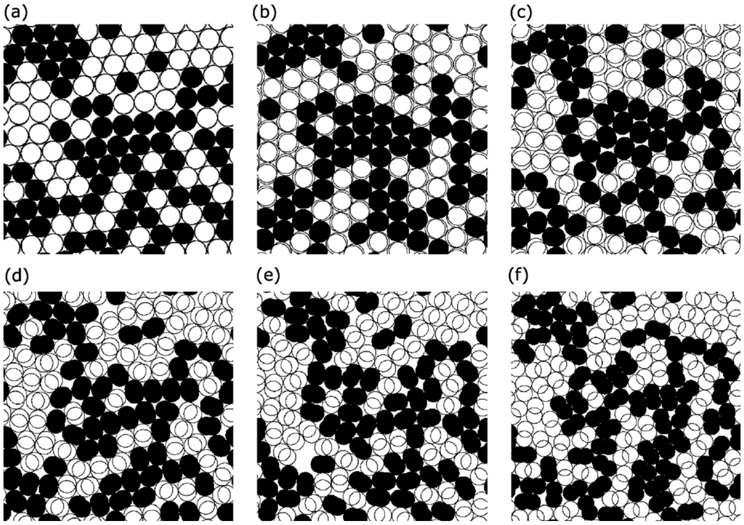

Figure 2.26 Jammed packings of $N = 256$ dimers with aspect ratios (a) $\alpha = 1.04$, (b) 1.1, (c) 1.2, (d) 1.3, (e) 1.4, and (f) 1.6. Corresponding global Q_6 values are plotted in Figure 2.25 (dashed line).

form polycrystals, which yield a low value of Q_6^g because the ordered domains are out of phase with each other. Similarly, uniaxial objects form nematic domains when quenched rapidly [56]. We will now review several spatial correlation functions that provide correlation lengths related to the size of ordered subregions.

We will first measure a spatial correlation length from the decay of correlations in $g(r)$. As we showed earlier in Figure 2.21, the fluctuations in $g(r) - 1$ die out

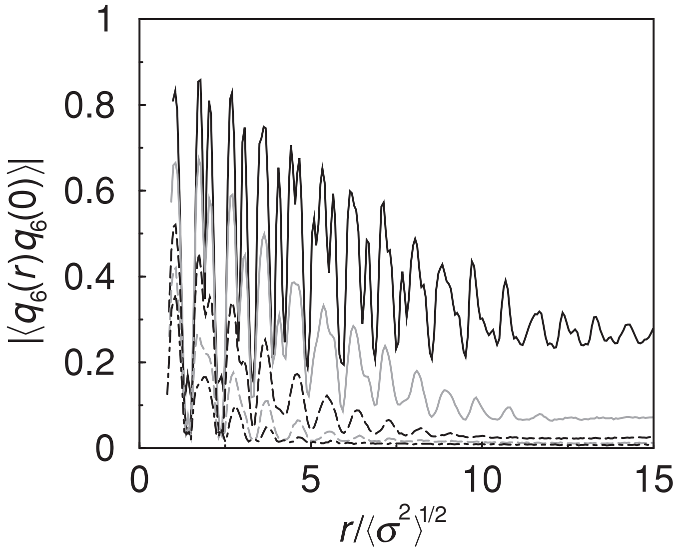

Figure 2.27 The magnitude of the complex Q_6 spatial correlation function for $N = 1024$ jammed disk packings with polydispersity $p = 1.1$ (solid black), 1.2 (solid gray), 1.3 (dashed black), 1.4 (dashed gray), and 1.5 (dot–dashed black).

quickly for fluid systems, less quickly for jammed systems, and persist over large distances for crystalline systems. In Figure 2.28(b), we plot the local maxima of $g(r) - 1$ for disk packings with different polydispersities. The decay of correlations is exponential with a correlation length ξ that grows with decreasing polydispersity as shown in Figure 2.29.

The Q_6 spatial correlation function also provides a correlation length related to fluctuations in particle positions [57]. Just as we defined Q_6^g and Q_6^l averaged over the whole system, we can also define q_6^i for each particle i. In 2D, $q_6^i = n_i^{-1} \sum_{j=1}^{n_i} e^{6\imath\theta_{ij}}$. We consider two spatial correlation functions formed from q_6^i: the complex Q_6 correlation function $\langle q_6(r)q_6(0)\rangle$ and the magnitude Q_6 correlation function $\langle |q_6(r)||q_6(0)|\rangle$. These correlation functions are calculated by choosing a bin size δr, binning all values of $q_6(r')q_6(0)$ (or $|q_6(r')||q_6(0)|$) between $r' = r$ and $r' = r + \delta r$, and then dividing by the number of pairs between r and $r + \delta r$. Since $q_6(r)q_6(0)$ is a complex number and contains phase information, the difference between these two correlation functions is analogous to the difference between the order parameters Q_6^g and Q_6^l. The complex Q_6 correlation function is sensitive to fluctuations in phase. Therefore, it should decay to $1/\sqrt{N_b}$ in an amorphous system, where N_b is the number of bonds, or $1/\sqrt{N_\mathrm{d}}$ in a polycrystal. In contrast, the magnitude Q_6 correlation function is not sensitive to fluctuations in phase.

In Figure 2.27, we show the magnitude of the complex Q_6 correlation function $|\langle q_6(r)q_6(0)\rangle|$ as a function of polydispersity for jammed disk packings.

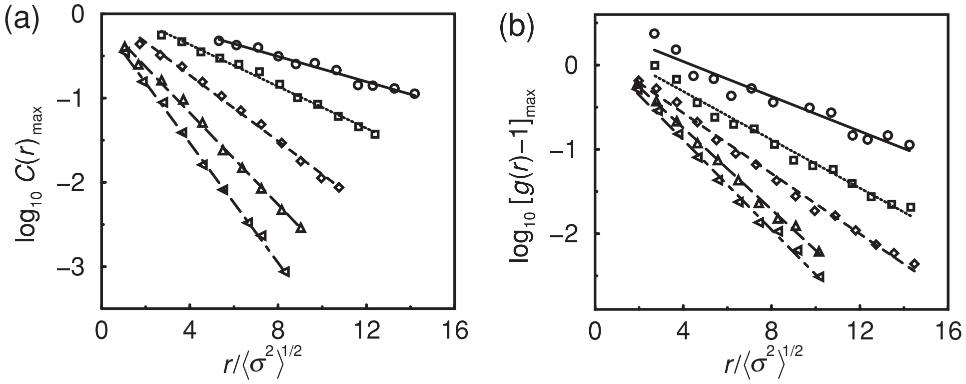

Figure 2.28 Local maxima of (a) $C(r)$ (defined in the text) and (b) $g(r) - 1$ for disk packings with polydispersities $p = 1.1$ (circles), 1.2 (squares), 1.3 (diamonds), 1.4 (upward triangles), and 1.5 (leftward triangles). The lines show least-square fits to $e^{-r/\xi}$.

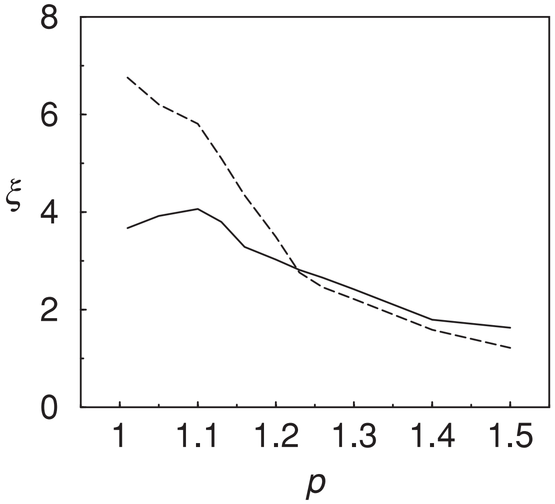

Figure 2.29 Correlation length ξ obtained from the decay of the local maxima of $C(r) = |\langle q_6(r)q_6(0)\rangle - \langle q_6(\infty)q_6(0)\rangle|$ (dashed line) and $g(r) - 1$ (solid line) shown in Figure 2.28 for disk packings as a function of polydispersity p.

$|\langle q_6(r)q_6(0)\rangle|$ decays more slowly as the polydispersity decreases due to the increase in polycrystalline domain size as shown in the snapshots in Figure 2.23(a) and (b). To extract a correlation length from the decay of correlations in Figure 2.27, we plot the local maxima of $C(r) = |\langle q_6(r)q_6(0)\rangle - \langle q_6(r)q_6(\infty)\rangle|$ in Figure 2.28(a). The correlations decay exponentially with distance over a lengthscale that increases with decreasing polydispersity p. The dependence of the correlation length from $|\langle q_6(r)q_6(0)\rangle|$ on p appears in Figure 2.29. Note that the

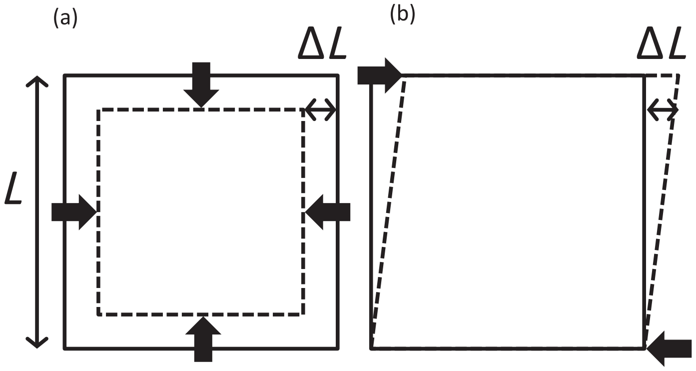

Figure 2.30 (a) Isotropic compression and (b) simple shear for strain $\gamma = \Delta L/L$.

lengthscales from the complex Q_6 and $g(r)$ correlation functions show a marked departure at low polydispersities.

4.5 Bulk and shear moduli

The mechanical properties of jammed systems are qualitatively different from those of crystalline solids. For example, in crystalline solids, the response to shear strain is generally comparable to the response to isotropic compression. However, in jammed, frictionless particulate systems, the response to shear is much weaker than that for isotropic compression. In this section, we will demonstrate this property by calculating the static bulk modulus, B, (response to isotropic compression) and shear modulus, G, (response to shear strain) for jammed frictionless packings.

To measure B (G), we slightly deform the system by applying an infinitesimal isotropic compressive (shear) strain as shown in Figure 2.30(a) (Figure 2.30(b)), allowing the system to relax, and then measuring the resulting isotropic (shear) stress in the system [13]. We perturb the system over a range of strains to verify that the measurements are in the linear response regime. The shear and bulk moduli are obtained by measuring the response of the pressure tensor, $P_{\alpha\beta}$ to the applied strain, where:

$$P_{\alpha\beta} = -L^{-d} \sum_{i>j} r_{ij\alpha} \frac{r_{ij\beta}}{r_{ij}} \frac{dV}{dr_{ij}} \tag{2.34}$$

and $\alpha, \beta \in \{x, y, z\}$. The bulk and shear moduli are defined by $B = \phi dP/d\phi$ and $G = d\Sigma/d\gamma$, where P is the pressure and $\Sigma = -P_{xy}$ is the shear stress (when x (y) is the shear (gradient) direction). In Figure 2.31, we show that Σ is linear in γ and P is linear in $\phi - \phi_J$ over several orders of magnitude in jammed disk packings.

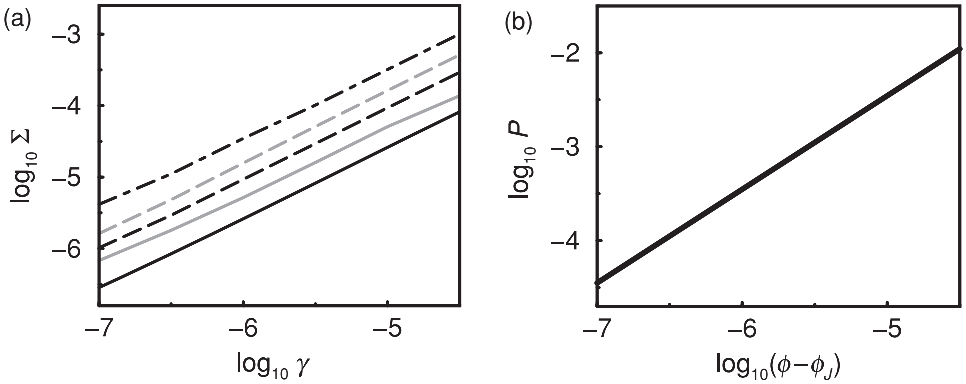

Figure 2.31 (a) Shear stress Σ versus shear strain γ in jammed disk packings at $\phi - \phi_J = 6 \times 10^{-5}$ (solid black), 3×10^{-4} (solid gray), 1×10^{-3} (dashed black), 4×10^{-3} (dashed gray), 2×10^{-2} (dot–dashed black). (b) Pressure P versus $\phi - \phi_J$ for jammed disk packings. P is linear in $\phi - \phi_J$, and Σ is linear in γ over several orders of magnitude.

The magnitude of the shear stress versus strain curve has strong $\phi - \phi_J$ dependence, showing a power law dependence $G \propto (\phi - \phi_J)^{1/2}$ [13]. In contrast, the bulk modulus does not depend strongly on $\phi - \phi_J$. Thus, in the limit $\phi \to \phi_J$, the bulk modulus remains finite, while the shear modulus goes to zero. This behavior has been related to the depletion of low frequency modes in the jamming density of states [58], [59], revealing fundamental physics not found in crystalline solids.

A subtle aspect of the shear modulus calculations especially for packings of spherical particles is the wide distribution of yield strains. In Figure 2.31, the yield strain $\gamma_y > 10^{-4}$ for all $\phi - \phi_J$ shown. However, γ_y even at fixed $\phi - \phi_J$ has large fluctuations, and thus for measurements on some configurations it is difficult to be simultaneously below the yield strain, above numerical noise, and within the linear regime. Several examples of nonlinear stress versus strain curves are shown in Figure 2.32. We have noticed that this behavior is diminished in large systems and systems composed of ellipsoidal particles.

Though B is nearly for same for jammed packings of ellipses and disks (Figure 2.33, main panel), G is much smaller for ellipses than for disks (Figure 2.33, inset). In fact, $G \propto (\phi - \phi_J)$ for ellipses at sufficiently low $\phi - \phi_J$, whereas $G \propto (\phi - \phi_J)^{1/2}$ for disks. For low aspect ratio ($\alpha < 1.01$), the $\phi - \phi_J$ scaling intersects the $(\phi - \phi_J)^{1/2}$ scaling for disks at $\phi^*(\alpha)$, below which the system has sphere-like $(\phi - \phi_J)^{1/2}$ scaling, and above which the system has $\phi - \phi_J$ scaling [33]. This new scaling behavior has been linked to quartic vibrational modes found in "just-touching" ellipse packings. Thus, near-jamming ellipse packings are much more susceptible to shear than packings of spherical particles.

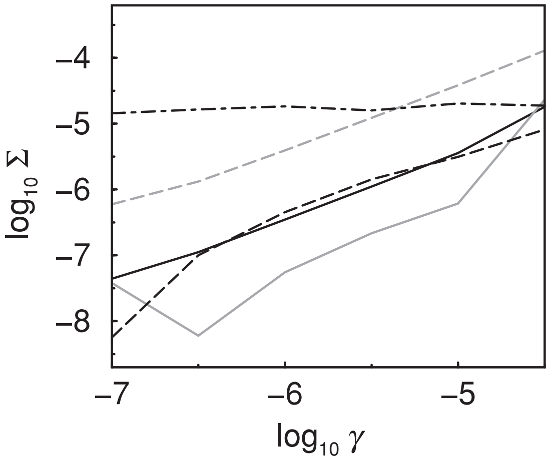

Figure 2.32 (a) Shear stress Σ versus shear strain γ for the same $\phi - \phi_J$ values in Figure 2.31. For some of these configurations, the yield strain is extremely small, which causes nonlinearity in $\Sigma(\gamma)$.

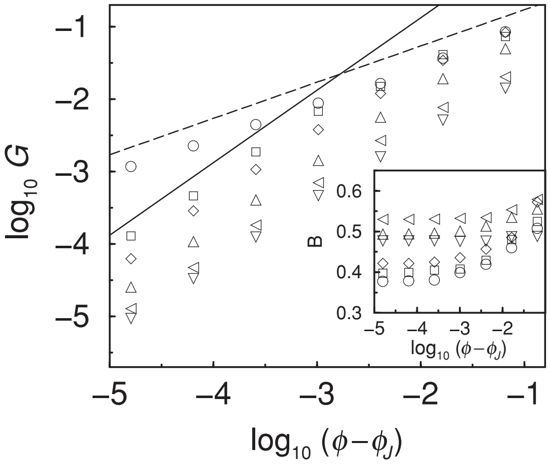

Figure 2.33 Shear (main plot) and bulk (inset) moduli versus $\phi - \phi_J$ for ellipse packings at $\alpha = 1.0$ (circles), 1.002 (squares), 1.01 (diamonds), 1.1 (upward triangles), 1.5 (leftward triangles), 2.0 (downward triangles). Notice that over the range $\phi - \phi_J = 10^{-5}$ to $\phi - \phi_J = 10^{-1}$, B changes by a factor of 1.5, while G changes by a factor of 100. The solid (dashed) line has slope 1 (0.5). Adapted from reference [33].

Acknowledgments

Support from NSF grant numbers DMR-0448838 (CSO) and DMS-0835742 (CS) is acknowledged. We gratefully acknowledge helpful discussions with Bulbul Chakraborty, Mitch Mailman, and Gregg Lois.

References

[1] S. Torquato, T. M. Truskett, and P. G. Debenedetti, "Is random close packing of spheres well defined?" *Phys. Rev. Lett.* **84**, 2064 (2000).
[2] N. Xu and C. S. O'Hern, "Measurements of the yield stress in frictionless granular systems," *Phys. Rev. E* **73**, 061303 (2006).
[3] W. Kob and H. C. Andersen, "Testing mode-coupling theory for a supercooled binary Lennard–Jones mixture I: the van Hove correlation function," *Phys. Rev. E* **51**, 4626 (1995).
[4] P. N. Pusey and W. van Megan, "Observation of a glass transition in suspensions of spherical colloidal particles," *Phys. Rev. Lett.* **59**, 2083 (1987).
[5] K. N. Pham, A. M. Puertas, J. Bergenholtz, S. U. Egelhaaf, A. Mousa ïd, P. N. Pusey, A. B. Schofield, M. E. Cates, M. Fuchs, and W. C. K. Poon, "Multiple glassy states in a simple model system," *Science* **296**, 104 (2002).
[6] L. E. Silbert, D. Ertas, G. S. Grest, T. C. Halsey, and D. Levine, "Geometry of frictionless and frictional sphere packings," *Phys. Rev. E* **65**, 031304 (2002).
[7] D. J. Durian and D. A. Weitz, "Foams," in J. I. Kroschwitz (ed.), *Kirk-Othmer Encyclopedia of Chemical Technology*, Vol. 11, p. 783, 4th edition (Wiley, New York, 1994).
[8] T. G. Mason, J. Bibette, and D. A. Weitz, "Elasticity of compressed emulsions," *Phys. Rev. Lett.* **75**, 2051 (1995).
[9] Z. Zhang, N. Xu, D. D. N. Chen, P. Yunker, A. M. Alsayed, K. B. Aptowicz, P. Habdas, A. J. Liu, S. R. Nagel, and A. G. Yodh, "Thermal vestige of the zero-temperature jamming transition," *Nature* **459**, 230 (2009).
[10] P. G. Debenedetti and F. H. Stillinger, "Supercooled liquids and the glass transition," *Nature* **410**, 259 (2001).
[11] A. Tanguy, J. P. Wittmer, F. Leonforte, and J.-L. Barrat, "Continuum limit of amorphous elastic bodies: a finite-size study of low frequency harmonic vibrations," *Phys. Rev. B* **66**, 174205 (2002).
[12] B. D. Lubachevsky, F. H. Stillinger, and E. N. Pinson, "Disks vs. spheres: contrasting properties of random packings," *J. Stat. Phys.* **64**, 501 (1991).
[13] C. O. O'Hern, L. E. Silbert, A. J, Liu, and S. R. Nagel, "Jamming at zero temperature and zero applied stress: the epitome of disorder," *Phys. Rev. Lett.* **68**, 011306 (2003).
[14] N. Xu, J. Blawzdziewicz, and C. S. O'Hern, "Reexamination of random close packing: ways to pack frictionless disks," *Phys. Rev. E* **71**, 061306 (2005).
[15] G.-J. Gao, J. Blawzdziewicz, and C. S. O'Hern, "Studies of the frequency distribution of mechanically stable disk packings," *Phys. Rev. E* **74**, 061304 (2006).
[16] A. Donev, R. Connelly, F. H. Stillinger, and S. Torquato, "Underconstrained jammed packings of hard ellipsoids," *Phys. Rev. E* **75**, 051304 (2007).
[17] W. S. Jodrey and E. M. Tory, "Computer simulation of close random packing of equal spheres," *Phys. Rev. A* **32**, 2347 (1985).
[18] R. J. Speedy, "Random jammed packings of hard discs and spheres," *J. Phys.: Condens. Matter* **10**, 4185 (1998).
[19] A. Zinchenko, "Algorithm for random close packing of spheres with periodic boundary conditions," *J. Comput. Phys.* **114**, 298 (1994).
[20] W. H. Press, B. P. Flannery, S. A. Teukolsky, and W. T. Vetterling, *Numerical Recipes in Fortran 77* (Cambridge University Press, New York, 1986).
[21] T. Majmudar and R. P. Behringer, "Contact force measurements and stress- induced anisotropy in granular materials," *Nature* **435**, 1079 (2005).

[22] S. Henkes, C. S. O'Hern, and B. Chakraborty, "Entropy and temperature of a static granular assembly: an ab initio approach," *Phys. Rev. Lett.* **99**, 038002 (2007).

[23] G. Lois, J. Xie, T. Majmudar, S. Henkes, B. Chakraborty, C. S. O'Hern, and R. Behringer, "Entropic origin of stress correlations in granular materials," submitted to *Phys. Rev. Lett.*, arXiv:0906.0056 (2009).

[24] S. Henkes and B. Chakraborty, "Statistical mechanics framework for static granular matter," *Phys. Rev. E* **79**, 061301 (2009).

[25] M. Lundberg, K. Krishan, N. Xu, C. S. O'Hern, and M. Dennin, "Comparison of low amplitude oscillatory shear in experimental and computational studies of model foams," *Phys. Rev. E* **79**, 041505 (2009).

[26] B. Miller, C. O'Hern, and R. P. Behringer, "Stress fluctuations for continuously sheared granular materials," *Phys. Rev. Lett.* **77**, 3100 (1996).

[27] M. P. Allen and D. J. Tildesley, *Computer Simulation of Liquids* (Oxford University Press, New York, 1987).

[28] G.-J. Gao, J. Blawzdziewicz, and C. S. O'Hern, "The nature of sheared mechanically stable granular packings," submitted to *Phys. Rev. E* (2009).

[29] D. J. Lacks and M. J. Osborne, "Energy landscape picture of overaging and rejuvenation in a sheared glass," *Phys. Rev. Lett.* **93**, 255501 (2004).

[30] B. A. Isner and D. J. Lacks, "Generic rugged landscapes under strain and the possibility of rejuvenation in glasses," *Phys. Rev. Lett.* **96**, 025506 (2006).

[31] G. Parisi and F. Zamponi, "Mean field theory of hard sphere glasses and jamming," to appear in *Rev. Mod. Phys.*, arXiv:0802.2180v3 (2009).

[32] L. Santen and W. Krauth, "Absence of thermodynamic phase transition in a model glass former," *Nature* **405**, 550 (2000).

[33] M. Mailman, C. F. Schreck, C. S. O'Hern, and B. Chakraborty, "Jamming in systems of ellipse-shapes particles," *Phys. Rev. Lett*. **102**, 255501 (2009).

[34] C. Schreck, J.-K. Yang, H. Noh, H. Cao, and C. S. O'Hern, "Pseudo band gaps in two-dimensional amorphous materials," unpublished (2009).

[35] D. Brown and J. H. R. Clarke, "Constant-stress nonequilibrium molecular dynamics: shearing of the soft-sphere crystal and fluid," *Phys. Rev. A* **34**, 2093 (1986).

[36] G.-J. Gao, J. Blawzdziewicz, C. S. O'Hern, and M. Shattuck, "Experimental demonstration of nonuniform frequency distributions of mechanically stable granular packings," submitted to *Phys. Rev. Lett.*, arXiv:0903.4941v1 (2009).

[37] Z. Zeravcic, N. Xu, A. Liu, S. Nagel, and W. van Saarloos, "Excitations of ellipsoid packings near jamming," submitted to *Europhys. Lett.*, arXiv:0904.1558v1 (2009).

[38] B. J. Berne and P. Pechukas, "Gaussian model potentials for molecular interactions," *J. Chem. Phys.* **56**, 4213 (1972).

[39] J. G. Gay and B. J. Berne, "Modification of the overlap potential to mimic a linear site–site potential," *J. Comp. Phys.* **74**, 3316 (1981).

[40] D. J. Cleaver, C. M. Care, M. P. Allen, and M. P Neal, "Extension and generalization of the Gay–Berne potential," *Phys. Rev. E* **54**, 559 (1996).

[41] J. W. Perram and M. S. Wertheim, "Statistical mechanics of hard ellipsoids I: overlap algorithm and the contact function," *J. Comp. Phys.* **58**, 409 (1985).

[42] J. W. Perram, J. Rasmussen, and E. Prætgaard, "Ellipsoid contact potential: theory and relation to overlap potentials," *Phys. Rev. E.* **54**, 6565 (1996).

[43] C. Schreck and C. S. O'Hern, "A new jamming critical point controls the glassy dynamics of ellipsoidal particles," unpublished (2009).

[44] S. Torquato and F. H. Stillinger, "Multiplicity of generation, selection, and classification procedures for jammed hard-particle packings", *J. Phys. Chem. B* **105**, 11849 (2001).

[45] C. F. Moukarzel, "Isostatic phase transition and instability in stiff granular materials," *Phys. Rev. Lett.* **81**, 1634 (1998).
[46] R. Blumenfeld, "Stresses in isostatic granular systems and emergence of force chains," *Phys. Rev. Lett.* **93**, 108301 (2004).
[47] H. A. Makse, D. L. Johnson, and L. M. Schwartz, "Packing of compressible granular materials," *Phys. Rev. Lett.* **84**, 4160 (2000).
[48] C. S. O'Hern, S. A. Langer, A. J. Liu, and S. R. Nagel, "Random packing of frictionless particles," *Phys. Rev. Lett.* **88**, 075507 (2002).
[49] W. Kob, C. Donati, S. J. Plimpton, P. H. Poole, and S. C. Glotzer, "Dynamical heterogeneities in a supercooled Lennard–Jones liquid," *Phys. Rev. Lett.* **79**, 2827 (1997).
[50] L. E. Silbert, A. J. Liu, and S. R. Nagel, "Structural signatures of the unjamming transition at zero temperature," *Phys. Rev. E* **73**, 041304 (2006).
[51] A. Donev, F. H. Stillinger, and S. Torquato, "Unexpected density fluctuations in jammed disordered sphere packings," *Phys. Rev. Lett.* **95**, 090604 (2005).
[52] K. E. Daniels and R. P. Behringer, "Hysteresis and competition between disorder and crystallization in sheared and vibrated granular flow," *Phys. Rev. Lett.* **94**, 168001 (2005).
[53] N. Duff and D. J. Lacks, "Shear-induced crystallization in jammed systems," *Phys. Rev. E* **75**, 031501 (2007).
[54] T. M. Truskett, S. Torquato, and P. G. Debenedetti, "Towards a quantification of disorder in materials: distinguishing equilibrium and glassy sphere packings," *Phys. Rev. E* **62**, 993 (2000).
[55] H.-J. Lee, T. Cagin, W. L. Johnson, and W. A. Goddard, "Criteria for formation of metallic glasses: the role of atomic size ratio," *J. Chem. Phys.* **119**, 9858 (2003).
[56] C. De Michele, R. Schilling, and F. Sciortino, "Dynamics of unixial hard ellipsoids," *Phys. Rev. Lett.* **98**, 265702 (2007).
[57] P. J. Steinhardt, D. R. Nelson, and M. Ronchetti, "Bond-orientational order in liquids and glasses," *Phys. Rev. B* **28**, 784 (1983).
[58] L. E. Silbert, A. J. Liu, and S. R. Nagel, "Vibrations and diverging length scales near the unjamming transition," *Phys. Rev. Lett.* **95**, 098301 (2005).
[59] W. G. Ellenbroek, E. Somfai, and M. van Hecke, W. van Saarloos, "Critical scaling in linear response of frictionless granular packings near jamming," *Phys. Rev. Lett.* **97**, 258001 (2006).